Advancing Photo(electro)chemical Water Splitting: The Promise of Atomically Dispersed Single-, Dual-, and Alloy-Site Catalysts

Maheswari Arunachalam,[(a)] Kwang-Soon Ahn,[(b)] Kai Zhu,[(c)*] and Soon Hyung Kang[(a)*]

[a]Department of Chemistry Education and Optoelectronic Convergence Research Center, Chonnam National University, Gwangju, 61186, South Korea

[b]Department of Chemical Engineering, Yeungnam University, Gyeongsan, 712-749, South Korea
[c]Chemistry and Nanoscience Center, National Renewable Energy Laboratory, Golden, CO, 80401, USA

*E-mail: skang@jnu.ac.kr (Soon Hyung Kang), kai.zhu@nrel.gov (Kai Zhu)

Keywords: Water splitting, HER, OER, Electrocatalyst, Single-atom catalyst, Dual-site single atom, Single-atom alloy

Single-atom catalysts (SACs) have rapidly gained prominence as an emerging class of electrocatalysts for water splitting, owing to their uniform and precisely defined active sites. By maintaining uniform reaction pathways, SACs minimize the formation of unwanted byproducts, thus exhibiting extremely high selectivity and atomic efficiency. A key determinant of SAC performance lies in the interfacial interaction between the isolated metal atoms and the supporting material under strong metal–support coordination which is vital for maintaining long-term activity. However, despite these benefits, the reproducibly synthesizing SACs with high metal loadings while retaining uniform dispersion remains a significant challenge. To address the intrinsic challenges of SACs, recent research has expanded into dual-atom catalysts (DACs) and single-atom alloy catalysts (SAACs), providing synergistic active sites and combining the benefits of SACs with bimetallic systems. This review systematically explores the latest advancements in synthesis methods and innovations for SACs for the electrochemical water splitting. Additionally, it examines the evolution of catalyst design, emphasizing the unique structural and electronic characteristics of single-site, dual-site, and alloyed SAC systems and highlighting their critical

roles in accelerating water-splitting reaction kinetics as well as the prevailing challenges and outlines promising directions for advancing hydrogen production via water electrolysis.

1. Introduction

Electrochemical water splitting is emerging as a scalable and efficient strategy for sustainable energy production.[1,2] This process enables the dissociation of water (H_2O) into high-purity hydrogen (H_2) and oxygen (O_2) through two key half-reactions: the hydrogen evolution reaction (HER, $2H^+ + 2e^- \rightarrow H_2$) and the oxygen evolution reaction (OER, $2H_2O \rightarrow O_2 + 4H^+ + 4e^-$).[3] This technology aligns well with global efforts to develop diverse energy solutions.[4] In complete water electrolysis, two coupled half-reactions proceed concurrently at physically separated electrodes submerged in an electrolyte. Under standard conditions, the theoretical minimum bias is fixed by the standard cell potential, $E°_{cell} = 1.23$ V. Classical thermodynamic parameters—Gibbs free energy (ΔG), enthalpy (ΔH), and the standard entropy change ($\Delta S° = +163.3$ J mol^{-1} K^{-1})—in concert with $E°_{cell}$ define the energetic threshold, constrain achievable efficiency, and determine the intrinsic spontaneity of the overall process.[5,6]

Although platinum-group metals set the benchmark for HER activity, their limited availability and high cost have driven intensive efforts to develop catalysts based on earth-abundant materials—most notably transition-metal dichalcogenides, hydroxides, and phosphides.[7-12] To overcome these limitations, one promising approach involves coupling trace amounts of platinum with water-affinitive transition-metal compounds to exploit interfacial synergy and accelerate HER kinetics. For example, Marković and colleagues coated Pt with a thin layer of nickel hydroxide ($Ni(OH)_2$), producing a hybrid catalyst whose HER activity exceeded that of conventional Pt alone.[13] Meanwhile, ruthenium and iridium oxides (RuO_2 and IrO_2) set the benchmark for oxygen-evolution catalysis (OER).[14,15] Their dependence on scarce noble metals, however, imposes high cost and scalability constraints. Consequently, identifying inexpensive materials capable of overcoming the inherently sluggish OER kinetics remains pivotal to advancing overall water-splitting efficiency.[16-23]

Reducing noble-metal catalysts to the single-atom scale vastly lowers precious-metal loading while preserving—or even enhancing—catalytic performance, thereby making the technology

economically attractive. In SACs, the isolated noble or first-row transition-metal centers are anchored on heteroatom-rich frameworks, including M–N, M–N–C, M–N–graphene, and emerging MXene lattices. Subtle alterations in these local coordination motifs can reshape the electronic structure of the active site, steering reaction pathways and modulating both activity and selectivity. Owing to this tunable atomic environment, SACs have demonstrated outstanding hydrogen- and oxygen-evolution activities, establishing them as some of the most promising materials for overall water splitting.

Isolated metal atoms tend to rapidly coalesce unless their dispersion is stabilized by coordinating ligands or robust supports. Accordingly, a detailed understanding—and deliberate manipulation—of the evolving coordination microenvironments of single atoms on oxide hosts is essential for the rational design of SACs. Even when isolated atoms are stabilised, OER performance can deteriorate because electron-donating intermediates bind too tenaciously to the transition-metal centres. This drawback stems from the inherent nature of single-atom sites: their adsorption free energies are governed by a single M–O interaction that offers little flexibility for electronic fine-tuning, which ultimately impedes efforts to lower the overpotential.[24] As recently reported, dual-atom sites can better stabilize intermediates during reactions like HER or OER.[25,26]

In general, dual-atom catalysts (DACs) featuring two adjacent single-atom active sites do not have a direct bond but are so close together on the support material that they interact electronically and catalytically. DACs offer superior performance compared to conventional SACs because they leverage the synergistic interaction between two neighboring metal atoms; these dual centers can collaboratively manage reaction intermediates, lowering energy barriers and facilitating faster reaction kinetics. The adjacent metal atoms provide complementary adsorption sites: One site can bind and activate a reactant while the other aids in subsequent bond formation or cleavage. This coordinated mechanism not only accelerates the overall reaction rate but also enhances selectivity by reducing undesired side reactions.[27-29] Fe-based DACs can enhance ORR catalytic activity by tuning the spin states of Fe through controlled bridging atoms. The Fe–O_2–Fe configuration exhibits superior performance due to its dual-metal active sites, which enables a bridging adsorption mode that strengthens oxygen molecule adsorption and promotes more efficient activation.[37] Carbon-free dual-atom catalysts (CFDACs) offer superior activity, selectivity, and stability over carbon-based DACs by avoiding carbon corrosion under harsh electrochemical

conditions. Using substrates like oxides, chalcogenides, or Xenes, CFDACs stably anchor dual-metal sites via O, S, B, or P ligands, ensuring durable performance in high-potential environments.[30]

DACs also face several challenges that must be addressed to reach their full potential. First, synthesizing DACs with precise atomic distances and configurations remains difficult, leading to variability in catalytic performance. Second, ensuring long-term stability under realistic operational conditions is crucial, as metal–metal bond breakage or metal migration can degrade their activity. Moving forward, advanced synthesis methods—such as atom-by-atom assembly and site-specific anchoring—will be pivotal for achieving precise, stable, and scalable DACs. As a result, recent advancements have focused on developing single-atom alloy (SAA) catalysts that address these challenges by combining the distinct advantages of isolated active sites with the improved stability and synergistic interactions offered by paired or alloyed metal atoms.

In this review, atomically dispersed catalysts—including single-atom (SAC), dual-atom (DAC), and single-atom alloy (SAA) systems—have greatly advanced electrochemical and photoelectrochemical (PEC) water splitting by improving atomic efficiency and controlling electronic structures at the atomic level. Precise synthesis methods such as atomic layer deposition, pyrolysis, and electrodeposition ensure good dispersion and stability, while doped carbon or oxide supports prevent aggregation. DACs use two adjacent atoms that work together to lower reaction barriers, and SAAs embed single atoms in metal hosts to combine high activity with strong durability. In electrocatalysts, Ru-, Ni-, Co-, and Pt-based SACs or SAAs show very low overpotentials and excellent stability for HER and OER, mainly due to optimized hydroxyl adsorption and strong electronic coupling. Dual-site catalysts like Ni–Co or Co–Fe further enhance charge transfer and reaction kinetics. For PEC water splitting, SACs integrated into photoanodes (TiO_2, $BiVO_4$, Fe_2O_3) or photocathodes (Cu_2O, Ni foam) improve light absorption, charge separation, and surface reactions through M–O or M–N bonding. Alloy and diatomic-site catalysts (e.g., NiPt, Ru–P) provide additional electronic tuning and stability.

Overall, atomic-scale catalyst design offers a powerful route toward efficient, durable, and scalable solar hydrogen production. Furthermore, advanced detection techniques, including in situ X-ray absorption spectroscopy (XAS), electron microscopy, and vibrational spectroscopy, have been widely used and summarized to monitor local coordination, oxidation states, and structural

evolution during catalysis. These tools reveal the reaction mechanisms at play such as hydrogen adsorption–desorption dynamics, intermediate formation, and redox-driven atomic rearrangements, providing direct evidence of active-site behavior. Collectively, atomic-scale catalyst engineering combined with real-time characterization establishes a unified pathway toward efficient, durable, and scalable solar-driven hydrogen production.

2. Single-Atom Catalysts

SACs, in which isolated metal atoms are uniformly dispersed on a support, enable maximum atom utilization by allowing each atom to act as an active site. This unique structural feature marks a paradigm shift in heterogeneous catalysis, offering clear advantages over conventional nanoparticle-based systems.[31] However, many OER catalysts—particularly those based on Earth-abundant elements—suffer from structural degradation under harsh oxidative conditions, leading to decreased activity and sluggish reaction kinetics. Although substantial progress has been made in developing electrocatalysts for both the HER and OER, achieving high overall water splitting performance combined with long-term stability remains a significant challenge. In this context, optimized SACs not only improve catalytic efficiency, but also offer considerable cost benefits, especially for precious metals, by significantly reducing the required metal loading.[32,33]

SACs possess distinctive geometric and electronic characteristics arising from the complete elimination of metal–metal bonding and the presence of strong metal–support interactions. This atomically dispersed configuration modulates adsorption energies, directing reactions along more favorable pathways and lowering kinetic barriers, thereby enhancing activity and selectivity. In particular, orbital hybridization strategies in SACs can precisely modulate their electronic structures, tailor geometric configurations, enhance catalyst stability, promote favorable interactions with reactants, and ultimately boost catalytic activity and efficiency.[34-37] In addition, the intimate anchoring of the isolated metal centers suppresses agglomeration and sintering—degradation modes that commonly plague nanoparticulate catalysts under demanding conditions—so SACs retain their performance over prolonged operation, reducing deactivation and replacement costs. The platform is highly tunable by judiciously choosing the metal center, engineering the support, and fine-tuning the interfacial electronic coupling, catalytic behavior can be customized for a wide spectrum of reactions, extending the reach of SACs technology across multiple energy-conversion applications.

2.1. Why Are Supports Important for Single-Atom Catalysts?

Isolated single atoms present an extreme surface-to-volume ratio, resulting in substantial surface free energy and, as a result, considerable thermodynamic lability.[39–41] Without neighboring metal atoms, the isolated single atoms possess dangling bonds and unfilled valence orbitals, driving them to lower their energy by adsorbing surrounding species or, more critically, by agglomerating into clusters or nanoparticles. Robust stabilization achieved through strong coordination with ligands or, more commonly, firm anchorage on solid supports is thus indispensable for preserving atomic dispersion. A broad range of host matrices, including metal oxides, heteroatom-doped carbons, and emerging two-dimensional substrates, has proven effectiveness. These supports supply dense, high-affinity binding sites that facilitate higher single-atom loadings, circectly translating into enhanced catalytic performance.

Furthermore, SACs can stabilize metal atoms through coordination with heteroatoms such as N, O, C, S, and P, each imparting distinct catalytic properties. For example, M–N bonds contribute to structural stability and efficient electron transfer, M–O offers tunable redox behavior, M–C enhances local electron density, and M–S facilitates intermediate adsorption. Mixed heteroatom combinations (M–N–C, M–N–O, and M–O–C) can enhance catalytic versatility, selectivity, and tailored performance.

To date, most research on SAC-based catalysts has focused on their high atom utilization and finely tunable catalytic mechanisms. However, the following key challenges remain to be addressed. (1) Isolated atoms tend to migrate and aggregate during synthesis or reaction conditions, leading to loss of activity and selectivity. (2) Complex synthesis routes often require precise and expensive techniques, such as atomic layer deposition or high-temperature pyrolysis, which are hard to scale. (3) Low metal loading can negatively affect catalytic efficiency, especially in reactions that require a high density of active sites. (4) The choice of support materials is critical, as they influence the electronic structure and stability of the metal atoms.

2.2. Synthesis Techniques for Single-Atom Catalysts

The synthesis of SACs is pivotal, as their exceptional catalytic performance arises from precise atomic dispersion and well-defined coordination environments. A well-designed synthesis strategy prevents metal atom aggregation, ensuring stability and uniform active sites. Strong

metal–support interactions, achieved through controlled synthesis, further boost activity, selectivity, and durability. Advanced methods—such as pyrolysis, atomic layer deposition (ALD), wet chemistry, and metal-organic framework (MOF)-derived approaches—enable the tailoring of coordination structures for specific reactions, including OER, HER, and CO_2 reduction reaction. Scalable and reproducible synthesis is crucial for practical applications, while efficient metal utilization minimizes the dependence on noble metals, thereby improving both cost-effectiveness and catalytic performance.

2.2-1. Preparation of Single-Site, Single-Atom Catalysts

Numerous fabrication routes have been developed for SACs, electrodeposition (ED),[42] atomic layer deposition (ALD),[43] chemical vapor deposition (CVD),[44] and photochemical reduction.[45-46] But, these techniques typically depend on advanced instrumentation and elaborate precursors, highlighting the demand for more straightforward, versatile synthetic protocols. Although the past decade has seen rapid advances, a universally applicable strategy that accommodates a broad range of metals and supports remains elusive and is now a focal point of catalytic research. In this section, we survey state-of-the-art methodologies for constructing single-site, dual-site, and alloy-type SACs. By affording precise control over atomic dispersion, local coordination, and electronic structure, these approaches yield catalysts with superior activity, durability, and selectivity, offering reproducible pathways toward well-defined SAC architectures. As a result, they are considered essential in overcoming the limitations of conventional catalysts and advancing the practical application of SACs in various catalytic processes.

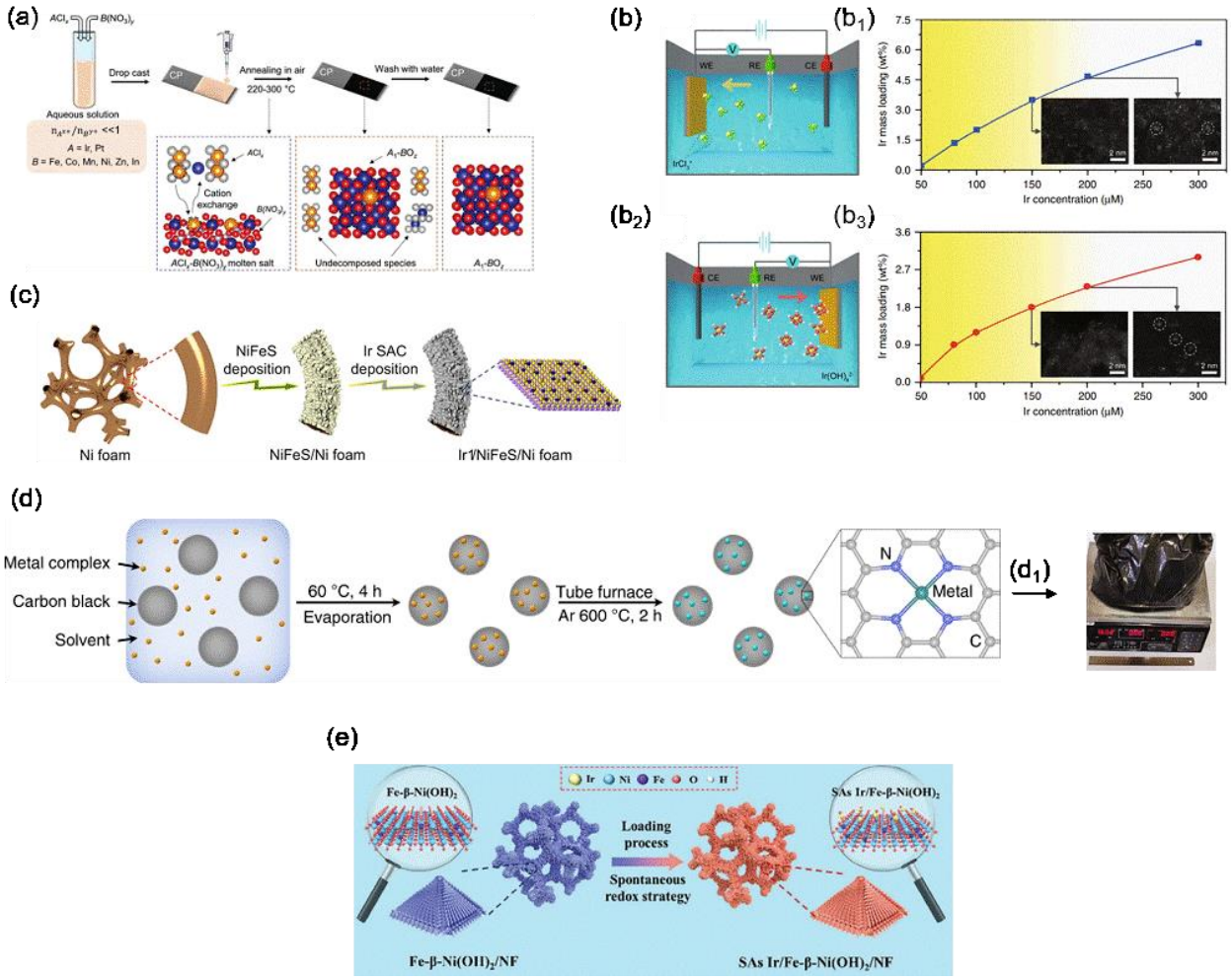

Figure 1. (a) Schematic overview of a generic synthetic pathway that yields single-site SACs based on both noble and first-row transition metals. Copyright 2024 Wiley-VCH [42]. (b–b_3) Cyclic-voltammetric electrodeposition of iridium: panels (b–b_1) depict cathodic deposition, whereas panels (b_2–b_3) show anodic deposition. In the molecular models, yellow, green, red and white spheres correspond to Ir, Cl, O and H atoms, respectively. (c) Two-step electrochemical protocol that immobilizes atomically dispersed Ir on Ni–Fe sulfide nanosheet arrays (Ir/NFS). Copyright 2022 Springer Nature [47]. (d) Universal two-stage strategy for fabricating metal SACs (M-SACs); inset (d1) photograph illustrates gram-scale production of Ni-SAC-2.5. Copyright 2019 Springer Nature [48]. (e) Redox-driven self-assembly route generating SAs-Ir/Fe-β-$Ni(OH)_2$ electrodes, wherein isolated Ir atoms are anchored on Fe-doped β-$Ni(OH)_2$ pyramid arrays. Copyright 2024, Wiley-VCH.[44]

Molten-salt pyrolysis has emerged as an attractive route to SACs, affording exceptional activity, selectivity, and durability. In this strategy, metal precursors are first fully solubilized in a molten-salt medium, creating an atomically homogeneous mixture. Subsequent high-temperature treatment decomposes the dissolved salts, liberating metal species as individual atoms. Xu et al. recently discloses a one-pot protocol that yields diverse noble-metal SAs anchored on non-noble metal oxides (Figure 1(a)). Their formulation employs trace noble-metal chlorides (ACl_X) together with abundant non-noble metal nitrates ($B(NO_3)_\gamma$). Upon mild calcination, the nitrates melt and convert to oxide supports (B–O), while the chlorides decompose to form isolated A–O entities. The molten state enhances ionic mobility, facilitating rapid cation exchange between the noble and base metals, which effectively stabilizes the former into atomically dispersed sites.

Zeng et al. developed a universal electrodeposition strategy that yields over thirty distinct single-atom catalysts (Figure 1(b)). Using cyclic voltammetry, atomically isolated metals can be anchored on a wide range of supports—including metal hydroxides, oxides, and selenides. Cathodic deposition, conducted between 0.10 and –0.40 V (Figure 1b–b_1), and anodic deposition, carried out from 1.10 to 1.80 V (Figure 1b_2–b_3), involve the hydrogen- and oxygen-evolution reactions, respectively, thereby imprinting different electronic states on the resulting SACs. For Ir precursors, a concentration of 150 μM produced truly atom-dispersed Ir sites with a 3.5 wt % loading. Increasing the concentration to 200 μM, however, surpassed the supersaturation threshold, triggering Ir nucleation into nanoclusters and only modestly raising the loading to 4.7 wt % (Figure 1b_1-b_3). These results revealed the paramount importance of maintaining the precursor concentration below the supersaturation threshold to keep single-atom dispersion.

A two-stage electrochemical protocol was developed to anchor atomically dispersed Ir on nickel–iron sulfide (NFS) nanosheet arrays, thereby eliminating bulk Ir deposition and maximizing exposure of active sites.[47] First, Ni foam was coated with ultrathin NFS nanosheets by cyclic-voltammetric deposition (–1.2 to +0.2 V vs Hg/HgO) from an electrolyte containing Ni/Fe salts and thiourea; the thiourea simultaneously supplied sulfur for nanosheet formation and chelated the Ir precursor, preventing its premature reduction. In a subsequent, narrower potential window, these chelated Ir species were selectively reduced and immobilized as single atoms on the pre-formed NFS scaffold (Figure 1(c)). This sequential strategy guarantees the efficient use of Ir, resulting in a catalyst with a high density of accessible, wee-defined active sites.

Zhang et al. introduced a "ligand-mediated" strategy to synthesize transition metal SAs supported on carbon, achieving high metal loadings (Figure 1(d)) and offering a scalable approach suitable for large-scale production.[48-49] Figure 140(d_2) shows the scalability of this method: A single batch yielded up to 1.6 kg of Ni-SAC.

A facile, bias-free galvanic exchange has been used to decorate Fe-doped β-$Ni(OH)_2$ pyramid arrays with atomically dispersed Ir (Figure 1(e)). First, a porous Fe-β-$Ni(OH)_2$ layer is grown on Ni foam via a self-templating conversion, furnishing a high-surface-area scaffold. Immersion of this electrode in an $IrCl_3$ solution then initiates a spontaneous redox couple: surface NiOOH species are reduced to $Ni(OH)_2$ via dehydrogenation ($NiOOH + e^- \rightarrow Ni(OH)_2 + H^+$), while Ir^{3+} ions are simultaneously reduced ($Ir^{3+} + xe^- \rightarrow Ir^{(3-x)+}$). The potential gap between these half-reactions drives the process without external assistance, and the oxygen-rich surface formed during dehydrogenation supplies abundant coordination sites that immobilise the initial Ir atoms. The resulting Ir/Fe-β-$Ni(OH)_2$/NF catalyst therefore combines high single-atom loading with robust anchorage, ensuring excellent stability and atom-utilization efficiency.[50-53]

2.2-2. Dual-Site Single-Atom Catalyst Synthesis

In the dual-site paradigm, two distinct atomic species are embedded in adjacent coordination sites, allowing each element to retain its intrinsic characteristics while their close-range coupling finely tunes the surface electronic structure. These findings emphasize the effectiveness of dual-site structures in directing reaction pathways, reducing undesirable side reactions, and facilitating efficient, multistep proton-coupled electron transfer processes.[54-56] Although dual-site architectures offer significant advantages in tuning surface states and reaction pathways, their practical realization remains challenging. In particular, it is difficult to isolate two distinct transition metals on the same support, largely due to the lack of precise control over atomic arrangements during high-temperature pyrolysis processes. To overcome this challenge, a molecular engineering strategy was applied to *g*-C_3N_4 to design both single- and dual-site SACs with enhanced bifunctional catalytic performance. Through the controlled pyrolysis, isolated single atoms of Ni, Co, and Fe—as well as dual Ni-Fe atomic sites—were successfully anchored onto N-doped graphene nanosheets (Figure 2(a)), achieving high metal loadings of up to 10 wt%. Guided by theoretical predictions, NiCo single-atom dimers (SADs) on N-doped carbon were synthesized through a two-step strategy. In the first step, Ni^{2+} and Co^{2+} ions were selectively

confined within polydopamine spheres formed via self-polymerization under alkaline conditions, yielding Ni^{2+}/Co^{2+} at polydopamine precursors. This spatial confinement is crucial for inhibiting the aggregation of metal ions into clusters or nanoparticles, ensuring their atomic-level dispersion. Next, the Ni^{2+}/Co^{2+} at polydopamine precursor was subsequently vacuum-annealed at 800 °C, yielding NiCo single-atom dimers (NiCo-SADs) embedded in a nitrogen-doped carbon matrix (NiCo-SAD-NC) without compromising the original morphology (Figure 2(b)). Nitrogen functionalities within the carbon lattice furnish high-affinity coordination sites that immobilise the isolated Ni and Co atoms, thereby directing the construction of the intended NiCo-SAD architecture.

Atomically dispersed Fe–Ni dual sites have been synthesized via a straightforward high-temperature gas-migration route (Figure 2(c)). Leveraging the simultaneous polycondensation and chelation tendencies of ferric- and nickel-chloride precursors, ultrathin layers were first generated by freeze-drying a mixed solution of $FeCl_3 \cdot 6H_2O$ and $NiCl_2 \cdot 6H_2O$. During subsequent pyrolysis, these films retained their morphology, yielding porous carbon nanosheets that host isolated, adjacent Fe and Ni centers (FeNiSAs/CN). Comparable dual-site architectures—such as Ni/Co, Co/Fe, and Mo/W pairs—can also be realized by (i) a multistep templating protocol, (ii) reverse-micelle–assisted pyrolysis, and (iii) a low-temperature wet-chemistry approach, respectively (Figures 2(d–f)).[57-59]

2.2-3. Synthesis of Single-Atom Alloys

Conventional SACs are hampered by low metal loadings and a strong tendency for isolated atoms to cluster together, which is a result of the Gibbs-Thomson effect. Single-atom alloys (SAAs) circumvent these drawbacks by embedding individual foreign atoms within a bulk metallic lattice. The host matrix stabilizes the guest atoms thermodynamically, enabling markedly higher loadings while suppressing sintering. Moreover, the electronic properties of the surrounding metal can be tailored to fine-tune the guest atom's electronic structure, thereby enhancing catalytic performance. With their precise active sites, unique electronic configurations, and nearly perfect metal utilization, SAAs not only exhibit exceptional electrocatalytic activity but also provide an ideal platform for elucidating the relationship between atomic structure and catalytic behavior.[60-61] To demonstrate these properties further, porous NiPt alloy nanosheets have been anchored on Ni foam through a sequential two-stage hydrothermal route. Initially, the Ni foam was

hydrothermally oxidized in an H_2O_2/urea solution at 180 °C for 24 h, generating ultrathin β-$Ni(OH)_2$ layers approximately 3.2 nm thick. A second hydrothermal step, employing a Pt precursor, followed by Ar/H_2 annealing, promoted in-situ alloying, giving 3.7 nm NiPt nanosheets—the slight thickness increase originating from lattice expansion upon Pt incorporation. Additionally, a PtCo single-atom alloy catalyst (PtCo-SAAC) supported on nitrogen-doped ultrathin carbon sheets was obtained through a one-pot pyrolysis protocol: homogeneous co-complexation of metal salts with organic ligands was followed by high-temperature carbonization, producing 1–2.8 nm PtCo alloy species atomically dispersed across the carbon scaffold (Figure 2(h)).

Figure 2(i) depicts a sequential route for constructing a dual-atomic Ru–Bi SAAs on graphene oxide (GO).[57] In the first stage, Ru^{3+} and Bi^{3+} ions chelate to the oxygenated functional groups of well-exfoliated GO under acidic conditions, yielding a GO–Ru/Bi adduct via O–Ru/Bi coordination. After freeze-drying, the powder is annealed at 900 °C in Ar and subsequently reduced in H_2/Ar. These thermal treatments trigger alloying, initially forming Ru–Bi nanoparticles. That is, because Bi possesses much lower melting and boiling points than Ru, Bi partially volatilizes during annealing, atomizing into isolated atoms. This process produces a hierarchical structure, in which Bi single atoms are found both within ~2.4 nm RuBi SAA nanocrystallites and as O-coordinated Bi sites on the graphene matrix. An analogous strategy produces a Ru–Co SAACs on N-doped carbon nanosheets (Figure 2(j)). One-pot pyrolysis of a Ru/Co heterometallic precursor with an N-rich ligand generates ultra-small RuCo alloy (1.5–4.0 nm) domains, intimately dispersed across the carbon support, while residual Co forms sub-nanometric clusters that cooperate with the alloyed Ru to optimize catalytic performance.[64]

In summary, the various synthesis methods play a critical role in shaping the structure of SACs, directly influencing their catalytic performance and selectivity. Techniques such as impregnation, ion exchange, and co-precipitation disperse metal ions onto supports with diverse pore structures, which affect metal–support interactions and electronic configurations. The stability and reactivity of these catalysts can be further optimized through ALD and CVD, both of which ensure uniform layer-by-layer growth. Additionally, pyrolysis-based methods using MOF precursors create porous carbon scaffolds that help stabilize single atoms and improve mass transport. Ultimately, the choice of synthesis method dictates the metal loading, coordination

environment, and stability of the SACs, thereby directly influencing their catalytic activity and selectivity.

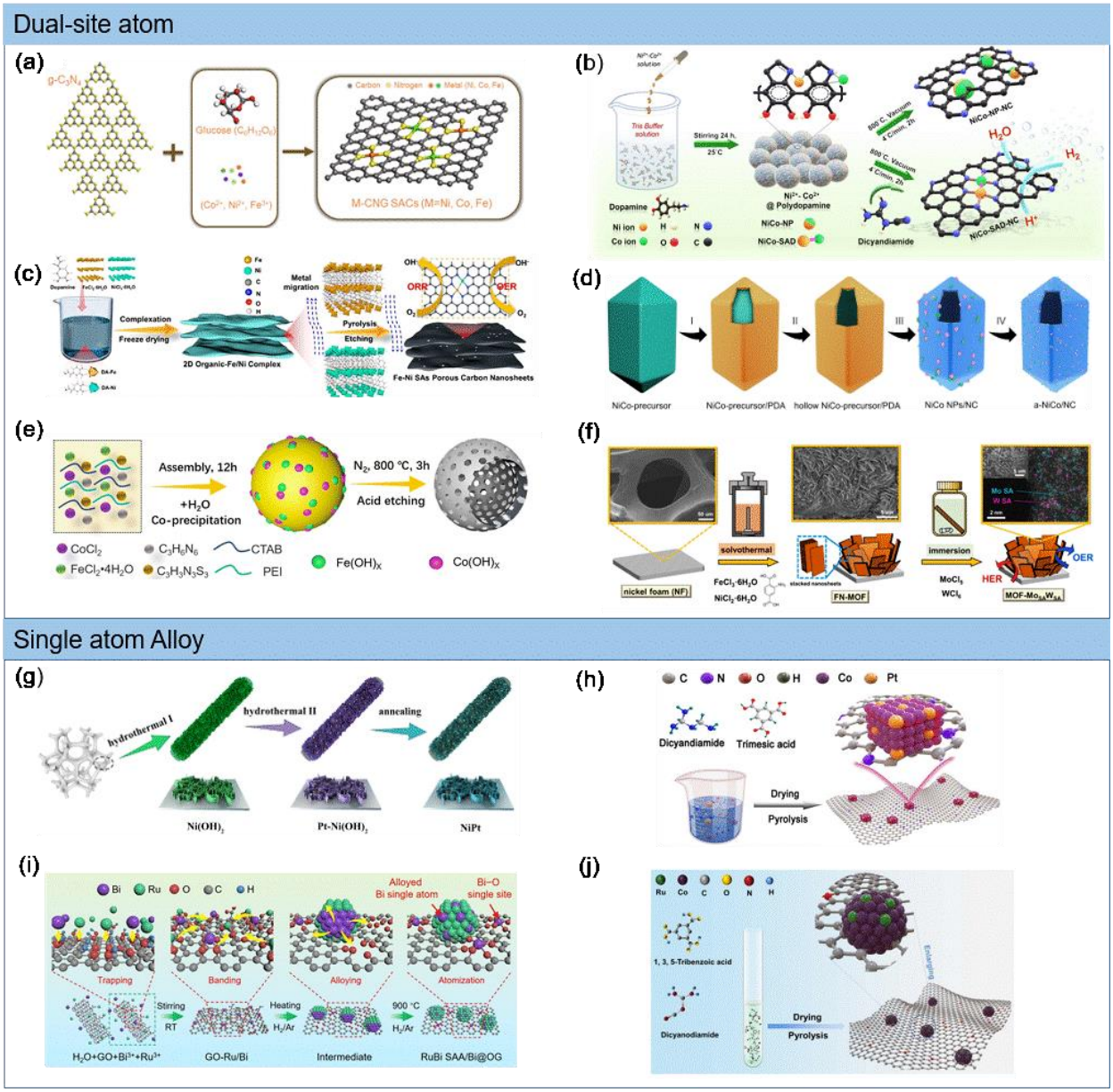

Figure 2. (a) Sequential schematic delineating a molecular-modification route that converts g-C_3N_4 and glucose into graphene-based single-atom catalysts (SACs). Copyright 2021 Springer Nature[54]. (b) Graphic rendering of the atomistic configuration for NiCo single-atom dimers embedded in N-doped carbon (NiCo-SAD/NC). Copyright 2024 Springer Nature[55]. (c) Conceptual diagram portraying the synthesis of FeNi single-atom sites on N-doped carbon (FeNi SAs/NC). Copyright 2024 American Chemical Society[56]. (d) Schematic overview of the

fabrication of atomically dispersed NiCo species anchored on N-doped carbon (NiCo/NC). Copyright 2022 Wiley-VCH[57]. (e) Diagrammatic workflow for constructing S- and N-coordinated Co/Fe-Co dual sites. Copyright 2023 Royal Society of Chemistry[58]. (f) Schematic depicting the assembly of a MOF-derived Mo single-atom/WS_2 hybrid (MOF-MoSA-WSA). Copyright 2023 Elsevier[59]. (g) Illustration of the synthetic process generating Pt single atoms on nickel nanosheets grown on Ni foam. Copyright 2022 American Chemical Society[61]. (h) Concept sketch of PtCo single-atom alloys dispersed on carbon nanosheets (PtCo SAA/CNs). Copyright 2024 Royal Society of Chemistry[62]. (i) Stepwise schematic for fabricating a RuBi single-atom alloy/isolated Bi site heterostructure on graphene oxide (RuBi SAA/Bi/GO). Copyright 2023 Wiley-VCH[63]. (j) Graphic illustration of the synthesis of RuCo single-atom alloys on N-doped carbon (RuCo SAA/NC). Copyright 2024, Wiley-VCH.[64]

2.4. Robust Recovery and Reuse Strategies for Single-Atom Catalysts

Reusability is vital in catalytic applications, especially for expensive SACs using noble metals like Pt, Pd, and Ir. It lowers the cost per cycle, reduces waste, and supports industrial scalability. The structural stability of SACs ensures high activity and selectivity over multiple uses, making them both efficient and durable. Most SACs are supported on solid materials such as nitrogen-doped carbon or metal oxides, or porous frameworks like ZIF-8. These solid supports not only provide stability to the catalysts, but also enable easy recovery after reactions. The catalysts can be efficiently separated from the reaction mixture using simple techniques, such as filtration, centrifugation, or decantation, making the recovery process straightforward and cost-effective. After separation, the catalysts can be washed, dried, and directly reused with minimal loss of performance. In addition to powder-based catalysts, thin-film SACs offer distinct advantages for reuse. Typically, catalysts immobilized on solid substrates such as glass, metal foils, or conductive supports can be easily regenerated through simple washing or mild treatment, without the need for physical removal. Moreover, thin films exhibit better structural integrity over multiple cycles and are less prone to material loss, reducing the risk of aggregation or leaching during repeated use and making them ideal for photoelectrochemical applications. Most SACs are supported on solid materials such as nitrogen-doped carbon, metal oxides or porous frameworks (ZIF-8), which not only anchor the single atoms but also facilitate easy recovery after reaction. For example, one

study of a binder-free SAC electrode (Ni/Au single-atoms on a doped nanocarbon) maintained almost unchanged over potential after 20,000 electrochemical cycles.[65]

A recent study revealed that the Pt_2/Fe_3O_4 SAC exhibits excellent catalytic activity in CO oxidation over multiple cycles, with minimal platinum aggregation or leaching. This innovative catalyst features isolated platinum atoms anchored to iron oxide nanocrystallites, resulting in remarkable stability and performance during CO oxidation as well as selective oxidation in hydrogen.[66]

3. Single-Atom Catalyst Characterization: Identification of the Electronic Structures of Single-Atom Catalysts

Catalytic process and reaction pathways of SACs are intrinsically governed by their atomic configurations and electronic features, both of which depend on the nature of the metal centers and their anchoring environments. Hence, atom-resolved insight is indispensable for the rational design and scalable synthesis of next-generation SACs. Aberration-corrected high-angle annular dark-field scanning transmission electron microscopy (AC-HAADF-STEM) and AC-STEM—unambiguously distinguish isolated metal atoms from nanoclusters and reveal their spatial arrangements. In conjunction, synchrotron-based X-ray absorption fine-structure spectroscopy (XAFS)—encompassing both extended (EXAFS) and near-edge (XANES) regimes—identifies the local coordination geometry and valence state of the active sites. Thorough fitting of these spectral data yields quantitative metrics, including bond lengths and coordination numbers, thereby furnishing a comprehensive atomic-scale blueprint of SAC architectures.

3.1 *In Situ* Characterizations for Mechanism Study

Photo(electro)chemical water splitting entails complex multi-step reactions and multi-electron transfer processes, making it challenging to understand the intrinsic reaction mechanism fully. Unraveling the structural evolution of active sites under real operating conditions is crucial, as it directly determines catalytic efficiency, reaction pathways, and the true nature of active species.[67]

In general, *ex situ* characterization provides only static snapshots before and after reactions, failing to capture the real-time structural and electronic evolution of catalysts. Consequently, it cannot accurately reveal the intrinsic electrochemical behavior or true structure–activity relationships under actual operating conditions, limiting insight into catalytic mechanisms.[68]

Meanwhile, *in situ* characterization enables real-time monitoring of catalysts under actual reaction conditions, capturing dynamic structural and electronic changes. By revealing morphology evolution, intermediate formation, and local coordination variations during operation, it provides essential insights into true active sites and reaction mechanisms, crucial for understanding and optimizing catalytic performance.[69] In recent years, advanced in situ characterization techniques have become essential for uncovering catalytic mechanisms in water splitting. Key methods include *in situ* Raman spectroscopy, X-ray absorption spectroscopy (XAS), and *in situ* operando imaging during SAC synthesis.[70-71]

3.1.1 *In Situ* Raman Spectroscopy

Raman spectroscopy is a vibrational spectroscopy that characterizes surface molecular structures by analyzing the inelastic scattering of light by molecules.[72] It can meet the high specificity and sensitivity of molecular structures in the low-frequency region while avoiding the interference of solvents on detection signals. Therefore, it can be used for in situ monitoring of oxygen-containing intermediates in electrocatalytic systems. By coupling *in situ* Raman microscope with a three-electrode electrochemical cell, vibrational spectra are collected while controlling the electrode potential using a potentiostat (Figure 3(a)). A potentiostat controlled the applied potential while Raman spectra were collected simultaneously. Excitation wavelengths of 532 or 633 nm were used for metal oxides and 785 nm for carbon-based catalysts to minimize fluorescence. All measurements were performed under potentiostatic or cyclic voltammetry conditions, and spectra were recorded after stabilization at each potential step for 30–60 s. The technique provides insights into bond vibrations, surface intermediates, and oxidation states, revealing active phase transitions (e.g., M-$(OH)_2$ → M-OOH, M$(OH)_2$ → MOOH) and identifying short-lived species such as *OOH or O–O during OER and M–H during HER.[73-74] Unlike *ex situ* analysis, *in situ* Raman directly correlates spectral evolution with electrochemical activity, enabling elucidation of dynamic structure–activity relationships and mechanistic understanding of the water-splitting process at the molecular level. In particular, recent studies on MoS_2-based SACs have demonstrated that *in situ* Raman can trace potential-dependent shifts (Figure 3(b)) in the E^1_{2g} and A_{1g} phonon modes, confirming the stability of the host lattice and charge redistribution around dopant sites. These changes correlate with hydrogen adsorption processes and validate the active-site participation of anchored metal atoms (Co in Co–MoS_2). Thus, *in situ* Raman spectroscopy bridges the gap between theoretical prediction and experimental observation, elucidating the structure–activity

relationship and guiding the rational design of highly efficient HER.[75]

Furthermore, Zhang *et al.* experimentally elucidated the electrocatalytic mechanism of NiFe LDH using *in situ* Raman spectroscopy. A series of potential-dependent Raman spectra for Au/NiFe LDH were recorded during a cyclic voltammetry sweep ranging from 1.12 to 1.44 V and back to 1.12 V (vs RHE), as shown in Figure 1(c). During the anodic sweep from 1.12 to 1.32 V, two distinct peaks at 462 and 535 cm^{-1} were observed, corresponding to the Ni–O vibrational modes of defective or disordered NiFe LDH nanocrystals. Upon further increasing the potential to 1.44 V, where oxygen evolution commences, these peaks vanished and two new bands emerged at 475 and 559 cm^{-1}, characteristic of NiOOH species. This spectral transformation indicates the electrochemical oxidation of NiFe LDH to NiOOH, confirming the dynamic structural evolution of active sites during OER, consistent with theoretical predictions of the NiFe LDH catalytic mechanism.[76]

3.1.2 In situ XAS

The X-ray absorption spectroscopy (XAS) technique has become a powerful and widely adopted tool for *in situ* investigations aimed at elucidating complex or ambiguous electrochemical processes. One of its major advantages is that it requires relatively simple instrumentation compared to other advanced spectroscopic methods. Figure 1(d) schematically presents typical electrochemical cells designed for *in situ* XAS measurements. In these configurations, the electrocatalyst layer is commonly deposited onto a porous carbon substrate, such as carbon paper or carbon cloth, which functions as the working electrode and ensures uniform electrochemical activity across the surface. To minimize electrolyte leakage while maintaining X-ray transparency, the cell's X-ray window is typically sealed with Kapton film.[77]

When operating in fluorescence detection mode, however, a key challenge arises in achieving a sufficiently high effective concentration of the absorbing element. Since the detector measures an averaged signal, merely increasing the electrocatalyst's mass loading can obscure valuable information with a strong background response. Therefore, maintaining a proper balance among the concentrations of the detected elements is crucial. In transmission mode, the incident X-rays pass directly through the electrolyte solution before reaching the detector. However, obtaining meaningful information from the electrocatalyst layer is often challenging because the electrolyte strongly absorbs X-rays, significantly reducing the transmitted intensity. To address this issue, in

situ electrochemical cells are typically designed with adjustable solution thicknesses, which are usually maintained at less than 1 mm to minimize attenuation and enhance signal quality. Furthermore, to mitigate the interference caused by bubble formation during electrochemical reactions, these cells are often equipped with a peristaltic pump system that continuously circulates the electrolyte, effectively removing generated gas bubbles and ensuring stable measurement conditions.[79]

The hydrogen adsorption strength plays a decisive role in determining HER performance, as supported by extensive theoretical and experimental evidence. In SACs, strong metal–support interactions can significantly influence hydrogen adsorption behavior, thereby modulating catalytic activity. In situ XAS has revealed that SACs undergo potential-dependent structural and electronic variations during HER. For instance, Fang et al. reported that Pt SACs with an initial $Pt_1–C_3N_1$ configuration transformed into low-coordinated, near-free Pt sites (Figure 3(e)). Under cathodic potentials, as evidenced by reduced coordination numbers and lower valence states, which facilitated stronger hydrogen adsorption and enhanced acidic HER activity. Likewise, Cao *et al*. identified the dynamic evolution of Co SACs under alkaline conditions, where the initial $Co_1–N_4$ structure converted into a high-valence $HO–Co_1–N_2$ species upon hydroxide coordination (Figure 3(f-h)), followed by water adsorption to form a $H_2O–(HO–Co_1–N_2)$ intermediate. The high-valence $HO–Co_1–N_2$ moiety was thus confirmed as the true HER active site (Figure 3(i)), highlighting the importance of identifying dynamic structural changes to establish accurate structure–activity relationships.[80]

3.1.3 In Situ/Operando Imaging during Synthesis

In situ/operando imaging during SAC synthesis and under reaction conditions enables a fundamental understanding of catalyst activation and degradation processes.[81] *In situ* imaging provides valuable insights into the mechanisms underlying SAC formation and enables the identification of stages where undesirable structural transformations occur. With the significant improvement in the temporal resolution of electron microscopy—through the development of direct electron detectors for TEM mode and faster scanning capabilities for STEM mode—it has become possible to capture rapid dynamic processes in real time To achieve such real-time observations under real environments, *in situ* TEM experiments are commonly conducted either within environmental TEM (ETEM) systems or by employing specialized holders. ETEM utilizes

a series of apertures and differential pumping to create regions of gradually varying vacuum while protecting the electron gun. However, this microscope design has inherent limitations due to the differential pumping setup. The gaseous environment cannot reach atmospheric pressure near the sample, reducing the reproducibility of benchtop reactions. Moreover, the series of apertures above and below the sample region restricts the detection angles of scattered electrons, thereby limiting the formation of high-quality HAADF images. To overcome these limitations, sealed gas cell holders have been developed, allowing controlled gaseous environments to be maintained around the sample while preserving imaging performance. A general schematic of such a gas cell holder is shown in Figure 3(j). For these holders, extensive miniaturization of the device components is required to fit within the microscope's pole-piece gap and maintain both mechanical stability and electron transparency. The application of such advanced *in situ* gas cell TEM techniques has enabled direct visualization of single-atom dynamics under reactive environments. For instance, DeRita *et al.* investigated the behavior of Pt SACs supported on anatase TiO_2 under various reducing and oxidizing environments, revealing *in situ* that the individual atoms exhibit dynamic mobility, as illustrated in Figure 3(k-l).[82] The use of TiO_2 nanoparticles with a diameter of approximately 5 nm facilitated the clear observation of single Pt atoms under these conditions. The Pt/TiO_2 system demonstrated stability under mild redox environments, where the isolated Pt atom (Pt_{iso}) was aligned with the Ti atomic column along the [021] zone axis. However, under harsh reducing conditions, the Pt atom became mobile, migrating across the TiO_2 surface, suggesting a reduction-induced weakening of the metal–support interaction.

Adding to this observation, Chen et al. employed the electron beam to deliberately initiate atomization, enabling direct monitoring of nanoparticle disintegration at the atomic scale. In their study, a truncated Ag nanoparticle supported on hollandite-type MnO_X with oxygen-terminated cavities capable of strongly trapping individual metal atoms was investigated under *in situ* conditions.[83] The truncated octahedral Ag nanoparticle gradually decreased in size while maintaining its morphology until it eventually vanished, as shown in Figure 3(m–n). This behavior indicates that Ag atoms diffuse via a classical surface-vacancy diffusion pathway, migrating layer by layer across the surface.[84] The complete disappearance of the Ag nanoparticle without reformation confirms that the oxygen-terminated cavities efficiently immobilize the metal atoms. *Ex situ* HAADF imaging further corroborated this finding, revealing that these trapping sites effectively prevent Ag atoms from re-aggregating into nanoparticles, regarded as an essential

factor for the stabilization of SACs.

While Chen *et al.* demonstrated beam-induced atomization at the atomic scale, subsequent studies sought to reproduce similar single-atom formation processes under more real thermal conditions. In related work that more closely simulates large-scale benchtop synthesis, Wei et al. employed in situ TEM to monitor the thermal conversion of noble metal nanoparticles into single atoms supported on N-doped ZIF-8.[85] When the sample was heated from room temperature to 1000 °C, the nanoparticles first coalesced and then gradually disappeared while the temperature was maintained at 1000 °C in an argon atmosphere. *In situ* imaging revealed that large Pd nanoparticles required extensive motion and collisions with the carbon support to disintegrate into single atoms, whereas smaller nanoparticles underwent atomization much more rapidly.

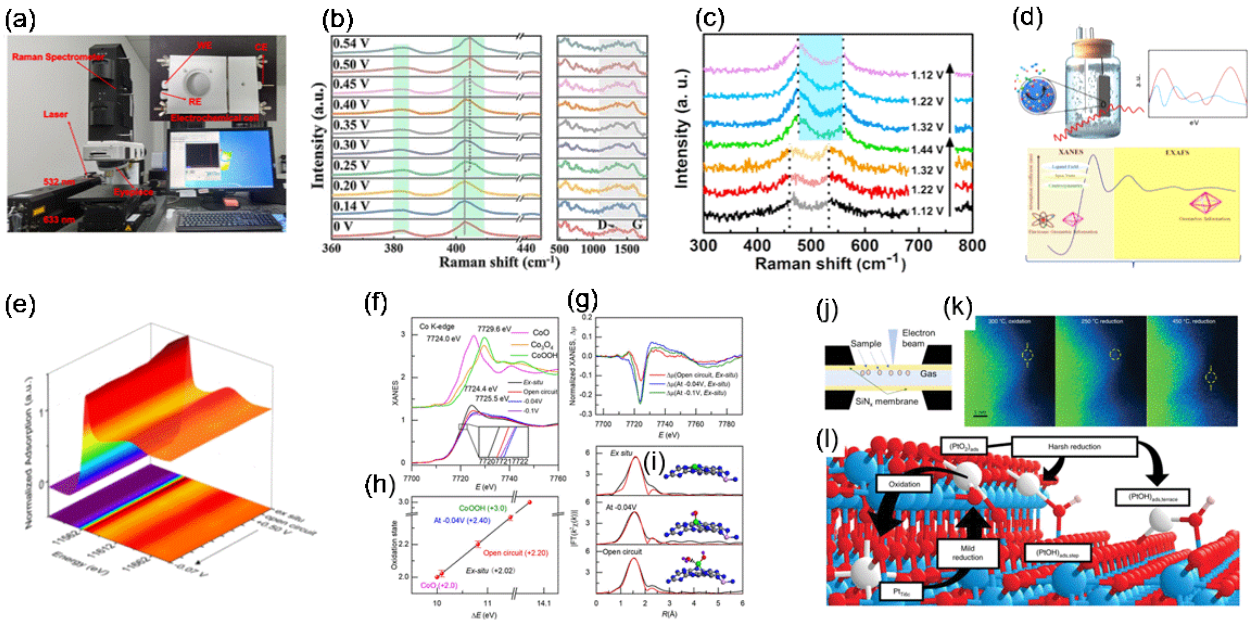

Figure 3. (a) Commercial laser confocal Raman microscopy system (WITEC alpha300R) together with the electrochemical reaction cell.[72] Copyright 2022 Nature Publishing Group.(b) *In situ* Raman spectra of the C−Co−MoS_2 SAC.[75] (c) Raman spectra of sAu/NiFe LDH at different potentials during anodic and cathodic sweep in a CV cycle.[76] (d) Experimental setup for *in situ* X-ray absorption spectroscopy.[77] (e) *In situ* XANES spectra of the Pt L_3 edge during the HER process.[78] (f-i) Identification of single-atom Co active sites during the HER process.[79] Copyright 2018 Springer Nature.(j) General schematic of the SiN_X viewing window inside *in situ* gas-cell TEM holder; (k) *In situ* HAADF images of Pt_{iso}/TiO_2 after 30 min under various annealing

conditions; and (l) Schematic illustrating the proposed dynamic evolution of Pt_{iso}/TiO_2 catalysts under oxidation, mild reduction, and harsh reduction conditions (from left to right, respectively).[81] Copyright 2019, Springer Nature.

3.2 DFT Computations

Density functional theory (DFT) studies have provided unprecedented insights into the HER and OER mechanisms by predicting catalytic activity through atomistic modeling. By constructing precise active-site and surface coordination models, DFT enables the identification of adsorption energies, reaction pathways, and energy barriers for key intermediates (H^*, OH^*, OOH^*, and O^*). Such theoretical analyzes guide the rational design and electronic modulation of catalysts with optimized hydrogen adsorption free energy (ΔG_{H^*}) for HER and favorable oxygen intermediate energetics for OER. Consequently, the integration of DFT predictions with experimental characterization provides a comprehensive understanding of structure–activity relationships, facilitating the targeted design of highly efficient and stable bifunctional electrocatalysts for overall water splitting.[86-87]

A recent study by Zhou *et al.* sought to establish clear design principles for bifunctional electrocatalysts by systematically evaluating a series of SACs, including Ni, Cu, Fe, Co, and Pd, embedded within nitrogen-doped graphene. Their investigation expanded to include a range of late transition metals anchored to graphene with different numbers of nitrogen coordination sites (termed xN–TM, where x ranged from 1 to 4).[88] A central finding was that the catalytic activity of cobalt (Co) was precisely determined by this coordination environment. For the HER, a low-coordinated cobalt site (specifically, a triple-coordinated 3N–Co) showed outstanding activity. It achieved a calculated hydrogen adsorption free energy ΔG_{H^*} of –0.01 eV, which is considered nearly ideal. For the OER, a high-coordinated cobalt center (a quadruple-coordinated 4N–Co) was the most promising candidate (Figure 4(a)). It demonstrated a low computed overpotential of –0.39 V. These performance metrics for both HER and OER are competitive with those of precious noble-metal catalysts. To understand the electronic origins of this behavior, the researchers employed computational methods like Partial Density of States (PDOS) and charge density difference analyses, focusing on the most stable 3N–Co and 4N–Co configurations. They also calculated the *d*-band center to correlate the electronic structure of the metal atoms with their HER

activity. This analysis revealed why the coordination number was so critical. The 3N–Co catalyst binds the OER intermediate HO* (hydroxyl) very strongly, which hinders the OER process. However, by increasing the coordination number to 4N–Co, the binding interaction with HO* is weakened (Figure 4(b–c)). This moderate binding strength is much more favorable for the OER pathway, resulting in the 4N-Co catalyst showing the best OER performance with a maximum energy barrier of only 1.61 eV (Figure 4(d-f)). In a related computational study, Wang's group also used DFT simulations to design a bifunctional SAC. They screened various transition metals on a TM1/β12-BM and identified the nickel atom (β_{12}-B-Ni) as the system with the best overall performance for total water splitting.[89]

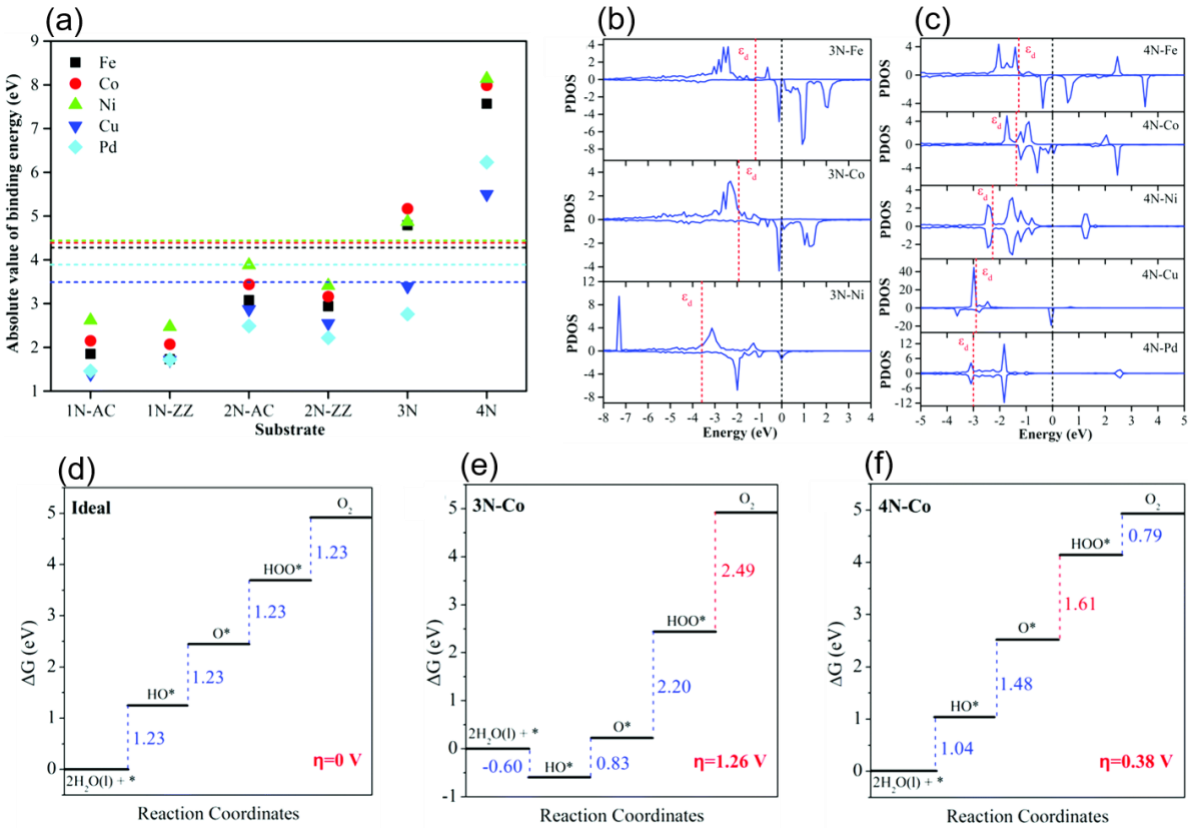

Figure 4. (a) Screening of the promising single atom catalysts with high geometric stability. The black, red, green, blue, and cyan lines correspond to the cohesive energies of Fe, Co, Ni, Cu, and Pd crystals, respectively. Copyright 2024, Royal Society of Chemistry[88] (b-c) Calculated PDOS of the *d* band of the TM. The Fermi level is set at the zero of energy, and the *d* band center (ε_d) is marked by the red dashed line. (d-f) Free energy diagram of OER on *x*N–TM at U = 0 V. The red line indicates the rate-determining step for OER. Copyright 2019, Royal Society of Chemistry.[89]

3.3. Comparative Analysis of SACs, DACs, and SAACs in HER and OER: Reaction Pathways, Adsorption Energies, and Active-Site Densities

SACs, DACs, and SAACs exhibit distinct catalytic behaviors in both HER and OER. SACs feature uniform active sites with strong metal–support interactions, leading to well-defined reaction pathways, but relatively low active-site density. DACs utilize the synergistic interaction between two adjacent metal atoms, optimizing intermediate adsorption energies and enabling more flexible reaction pathways. SAACs integrate the advantages of both isolated and alloyed configurations, fine-tuning adsorption through alloy effects and improving electrical conductivity. Overall, SACs excel in selectivity, DACs achieve balanced intermediate binding, and SAACs offer superior activity due to enhanced electronic modulation and higher active-site accessibility. A comparative summary of Table 1 revealed reaction pathways, adsorption energies, and active-site densities provided below.

Table 1. Summary of reaction pathways, adsorption energies, and active-site densities SACs, DACs, and SAACs in HER and OER.

Aspect	SACs	DACs	SAACs/SAAs
Active site	Isolated M–N_X, M–O_X, or M–C_X on supports	Binuclear M–M′ bridged via N-O-C on supports; controlled with M–M distance	Single dopant atom (e.g., Pt, Pd, Ru, Ni) diluted in host metal (e.g., Cu, Au, Ag, Ni)
Active-site Density	High atom efficiency, limited loading to avoid aggregation, and the highest activity per gram of noble metal.	Lower per gram than SACs (two metals/site) but can be similarly dense on high-loading supports	Very high geometric density (bulk surfaces), but true active dopant density is low (ppm–at.%); tunable via alloying
HER: pathways	Volmer–Heyrovsky most common on non-Pt SACs; Volmer–Tafel possible if $^*H$ can hop between nearby hetero sites on support	Enables bimetallic Volmer–Tafel with adjacent sites: one site favors $^*H$ formation (Volmer), neighbor lowers $^*H$–$^*H$ coupling barrier (Tafel)	Pt-group SAAs on late-metal hosts often favor Volmer–Heyrovsky with near-optimal $^*H$ on the dopant and facile water dissociation assisted by host
HER: intermediates	H on single site; $\Delta G_{[H^*]}$ near 0 eV desired; water dissociation barrier matters in alkaline	$^*H$ split across two metals; cooperative water activation	Dopant provides H site; *host tunes* $\Delta G_{[H^*]}$ and lowers water-dissociation barrier
HER: adsorption energy	Often too strong or too weak binding; coordination (N/O) tunes toward $\Delta G_{[H^*]} \approx 0$	At Volmer vs Tafel steps, one metal strengthens, the other weakens H to reach $\Delta G_{[H^*]} \approx 0$ and low coupling barrier	SAAs usually moderate H (closer to $\Delta G_{[H^*]} \approx 0$) by diluting Pt-group atom in inert host; suppresses H overbinding and poisons

HER: effect on kinetics	Excellent when $\Delta G_{[H^*]}$ tuned; may be mass-transfer limited at very high site utilization	Frequently lower overpotential via dual-site synergy; can beat single-site scaling on kinetic barriers	Industrially relevant exchange currents at ultralow PGMs; robust, CO-tolerant variants common
OE: dominant pathways	Adsorbate Evolution Mechanism (AEM): $^*OH \rightarrow {}^*O \rightarrow {}^*OOH \rightarrow O_2$ on a single site; some supports allow lattice-oxygen (LOM) at high potentials	True dual-site AEM/bi-functional: one site stabilizes $^*O/^*OH$, the other facilitates *OOH or direct $^{**}O–O$ coupling; partial scaling-relation relief	Metallic SAAs are less common for OER; when oxidized behavior resembles SACs but host can modulate electron density and conductivity
OER: intermediates	$\Delta G_{[OOH^*]} - \Delta G_{[OH^*]}$ scaling (~3.2 eV typical) inherently defines the minimum possible overpotential	Separate descriptors for the two metals and facilitates bifunctional mechanisms with lower theoretical η	If surface reconstructs to M–(oxy)hydroxide islands, descriptors revert to SAC-like; host improves charge transport
OER: adsorption energy	Single-site scaling often forces a compromise: optimizing $^*O$ weakens $^*OOH$ (or vice versa)	Can break/relax scaling by distributing intermediates across two sites; enables lower ΔG steps and reduced theoretical overpotential	Limited ability to break scaling unless dual ensembles form (less typical); tuning mainly via electronic/strain from host
Selectivity and side-reactions	High selectivity (single site); risk of over-oxidation or dissolution if not strongly anchored	Selectivity maintained; composition/geometry control needed to avoid M–M sintering	High poison tolerance; host dilutes dopant to suppress deep adsorption (e.g., S, CO)
Stability	Strong M–support bonds; risk of migration/leaching at harsh OER	Two-atom motifs are more aggregation-prone and require rigid anchoring	Alloy matrix stabilizes dopant; surface segregation possible—requires pretreatment/control

4. Nobel Metal and Transition Metal Single-Atom Electrocatalysts for Hydrogen Evolution Reaction

This section highlights recent progress in atomically dispersed electrocatalysts for the HER/OER, emphasizing single-site, dual-site, and alloy configurations that incorporate noble and transition metals. In particular, this section discusses the influence of structural, electronic, and coordination environments on catalytic activity, stability, and selectivity, providing insight into the fundamental factors that drive catalytic performance.

4.1. Single-Atom Catalysts for Hydrogen Evolution Reaction

4.1-1. Single-Atom Catalysts: Overcoming the Hydroxyl Adsorption/Desorption Barrier

In a SA electrocatalyst, the reaction is generally localized at specific "active sites" on the catalyst surface. When these sites exhibit an excessively strong affinity for hydroxyl (OH) species, the OH molecules adhere to the surface, hindering the adsorption of other essential reactants such as water molecules or protons. This issue is particularly critical during cathodic HER conditions, as the persistent binding of OH species effectively blocks the active sites, reducing the overall efficiency of hydrogen production.

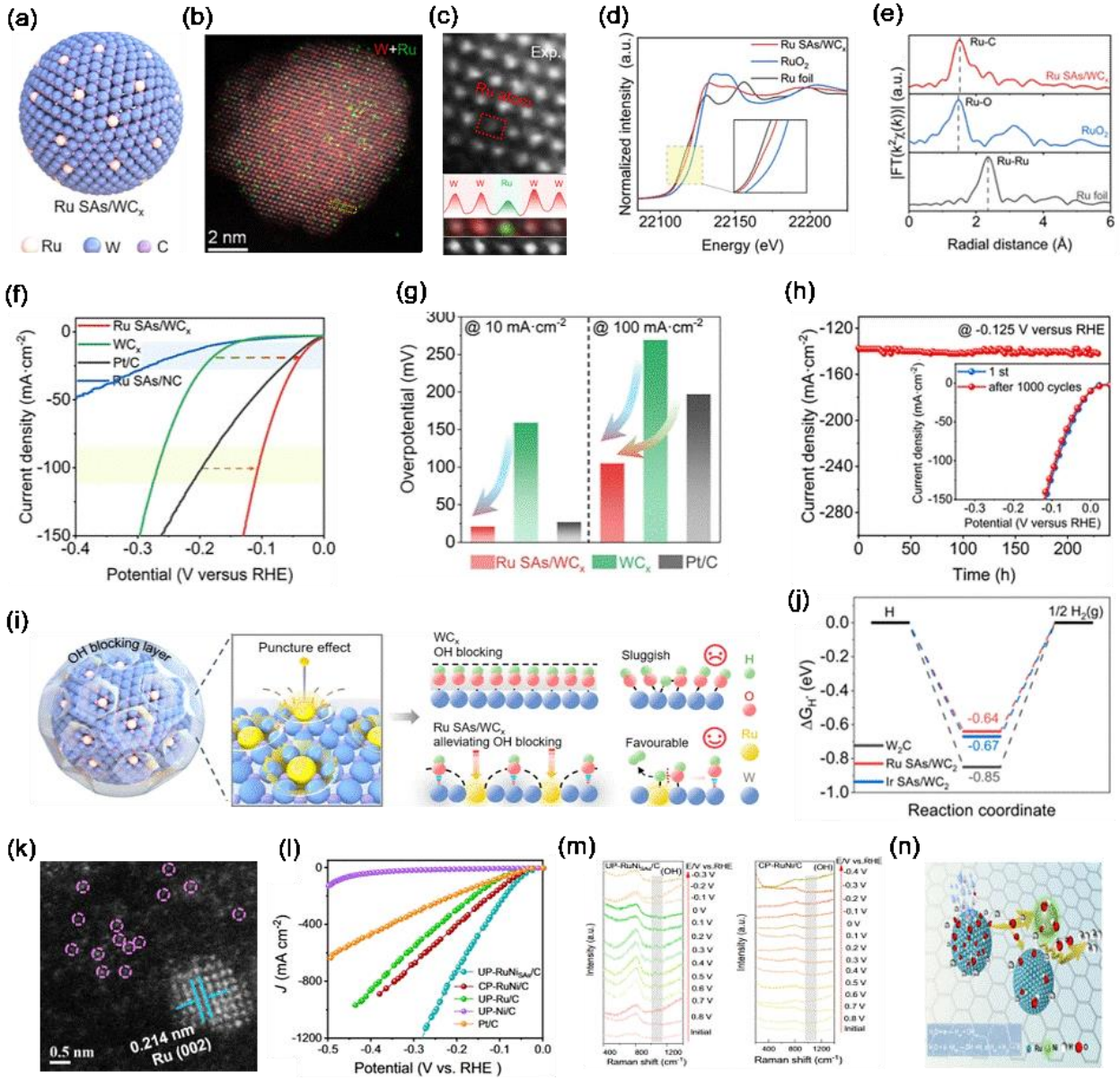

Figure 5. (a) Conceptual diagram outlining the step-by-step preparation of Ru single atoms anchored on tungsten carbide (Ru SAs/WC_x). (b) Atomically resolved STEM-EDS maps

confirming homogeneous Ru dispersion within WCx nanocrystallites. (c) Magnified STEM micrograph and corresponding intensity line-scans highlighting isolated Ru atoms. (d) Ru K-edge XANES spectra; (e) R-space EXAFS profiles comparing Ru SAs/WC_x with RuO_2 and metallic Ru. (f) Hydrogen-evolution polarization curves; (g) bar chart contrasting overpotentials for Ru SAs/WC_x, bare WC_x, and commercial Pt/C at 10 mA cm^{-2}. (h) Chronopotentiometric stability trace recorded at a fixed overpotential of 125 mV in 1.0 M KOH; inset: LSVs before and after 1 000 cycles. (i) Schematic illustration of the "puncture effect" whereby Ru single atoms disrupt OH-blocking layers on WC_x; (j) DFT-calculated Gibbs free energies for H^* adsorption on Ru- and Ir-decorated WC_2 versus pristine WC_2 (copyright 2024, American Chemical Society [58]. (k) Aberration-corrected STEM image showing atomically dispersed Ni sites (bright spots circled in pink). (l) Polarization curves of ultrafast-plasma (UP)-derived Ni/C, UP-Ru/C, chemically pyrolysed (CP) RuNi/C, UP-RuNi SAC on carbon (UP-RuNi SAs/C), and Pt/C benchmarks. (m) Operando Raman spectra comparing UP-RuNi SAs/C and CP-RuNi/C under catalytic bias. (n) Proposed reaction pathway for the UP-RuNi SAs/C system, highlighting synergistic Ru–Ni single-atom sites. Copyright 2024, Springer Nature.[90]

A recent study revealed that single-atom catalysts can produce a "puncture" effect, which significantly mitigates the blockage of active sites by OH species, thereby substantially enhancing HER performance under alkaline conditions. Tungsten carbides (WC_x) were selected as the ideal support (Figure 5(a)) for anchoring Ru SAs due to their unique electronic structure, which closely resembles that of Pt. Elemental mapping via HAADF-STEM (Figure 5(b-c)) shows that Ru atoms are uniformly distributed within the WC_x matrix, appearing as distinctly darker signals compared to the brighter tungsten atoms. Moreover, the similarity in interatomic distances between W–Ru and W–W pairs confirms that Ru atoms substitute some W atoms rather than forming clusters. Figure 5(d) presents the Ru K-edge XANES spectrum of the Ru SAs/WC_x sample shows an absorption edge nearly identical to that of Ru foil, although it is shifted to lower energy compared to RuO_2. This indicates that the Ru atoms in the electrocatalyst predominantly exist in a metallic state (or very close to it) rather than as oxidized species. In addition, maintaining a metallic state ensures that the electron density around the Ru atoms is sufficient to drive the water dissociation reaction, which is a key step in overcoming the challenge of OH blocking on catalyst surfaces. Moreover, Figure 5(e) contains the Fourier transform of the EXAFS spectra (in R-space) for the

Ru SAs/WC_x catalyst and for several reference materials, showing a single dominant peak near 1.51 Å attributed to Ru–C bonds. This key finding indicates that the Ru atoms are coordinated primarily with carbon atoms from the WC_x support and not with other Ru atoms, confirming their atomic dispersion within the lattice. The absence of peaks corresponding to Ru–Ru bonds rules out the formation of Ru clusters or nanoparticles, ensuring that nearly every Ru atom serves as an active catalytic site.

Figure 5(f) presents HER polarization curves measured in 1.0 M KOH, which indicate that the Ru SAs/WC_x catalyst achieves a current density of 10 $mA \cdot cm^{-2}$ at an ultralow overpotential of 21 mV, markedly outperforming the bare WC_x support, which requires 159 mV. This notable enhancement highlights the crucial role of atomically dispersed Ru sites in reducing the energy barriers associated with the HER. Figure 5(g) presents a quantitative comparison of overpotentials at -10 $mA \cdot cm^{-2}$ and -100 $mA \cdot cm^{-2}$. It clearly demonstrates that the Ru SAs/WC_x catalyst achieves lower overpotentials at higher current densities—105 mV at 100 $mA \cdot cm^{-2}$—compared to both the WC_x support and benchmark catalysts such as commercial Pt/C. Figure 5(h) compares the durability, demonstrating that Ru SAs/WC_x maintains stable operation over 220 h with negligible decay, and cyclic voltammetry tests (with 1,000 cycles) reveal virtually no negative shift in potential. This excellent stability confirms that the atomically dispersed Ru not only enhances initial activity, but also preserves HER performance under extended operational conditions—a critical requirement for practical, industrial-scale HER devices.

Figure 5(i) schematically illustrates the "puncture effect" induced by SA Ru on WC_x, where strong OH adsorption on pure WC_x creates a continuous blocking layer that limits active sites for HER. The incorporation of isolated Ru atoms weakens OH adsorption locally, effectively puncturing this layer and exposing additional active centers that promote both water dissociation and OH desorption. Complementing this, Figure 5(j) shows that the calculated Gibbs free energy of hydrogen adsorption (ΔG_{H^*}) on WC_2 models is moderate——0.64 eV for Ru and –0.67 eV for Ir—near the optimal range for efficient HER. Together, these findings reveal a synergistic mechanism in which the "puncture effect" clears interfering OH species while favorable hydrogen adsorption energetics ensure efficient reaction steps, yielding enhanced HER performance.[64]

4.1-2. Ni Single-Atom Catalysts: Engineering of Hydroxyl Adsorption for Robust Hydrogen Evolution Reaction Performance

Ru mediates the strong adsorption of OH intermediates, which can lead to site blockage and kinetic limitations. To overcome this, a recent study explored the synergistic modification of Ru nanocrystals with Ni_{SAs} anchored on a defective carbon support, creating an optimized interfacial structure that improves water dissociation and intermediate desorption. In this study, Ni_{SAs} anchored on defective carbon (especially at the zigzag-like graphene edge) yield the weakest OH adsorption energies. This moderated adsorption is crucial for facilitating rapid water dissociation and ensuring that the subsequent desorption of intermediates is not impeded.

The pulse-controlled deposition process (UPED) enables precise tuning of catalyst composition and nanostructure, yielding ultra-small Ru nanoparticles linked to atomically dispersed Ni via carbon bridges. This configuration optimizes the adsorption of intermediates, like OH, to boost high-current-density HER performance. In contrast, the chronopotentiometry (CP) method results in RuNi alloy nanoparticles. The AC-HR-TEM in Figure 5(k) reveals bright, well-defined Ru nanocrystals (~2 nm, corresponding to the (002) plane of hexagonal Ru) distinctly separated by lower-contrast Ni SAs, confirming the intended architecture, where Ni effectively modifies the Ru nanocrystals.

Figure 5(l) shows the polarization curves, highlighting the ultralow overpotentials of UP-RuNiSAs/C—attaining 9 mV at 10 $mA \cdot cm^{-2}$. Compared to Pt/C, this reflects superior HER kinetics, enhanced water dissociation, and an optimized active site design, thereby demonstrating excellent electrochemical activity.

Figure 5(m) illustrates the crucial operando insights and the underlying reaction mechanism for the UP-RuNiSAs/C catalyst in HER. Operando Raman spectroscopy reveals that the characteristic OH stretching band appears at more positive potentials for UP-RuNiSAs/C than for CP-RuNi/C, indicating accelerated water dissociation and rapid OH intermediate desorption. This facilitates efficient removal of intermediates that are crucial for high current densities. Figure 5(n) presents a schematic showing the synergistic interaction between Ru nanocrystals and Ni single atoms (Ni_{SAs}) through defective carbon bridges, describing how Ni_{SAs} enhance water decomposition at Ru sites while optimizing the adsorption-desorption dynamics of the OH

intermediates. This dual functionality minimizes excessive OH accumulation that could block active sites, significantly boosting HER kinetics, stability, and overall catalyst performance.[90]

4.2. Dual-Site Catalysts for Hydrogen Evolution Reaction

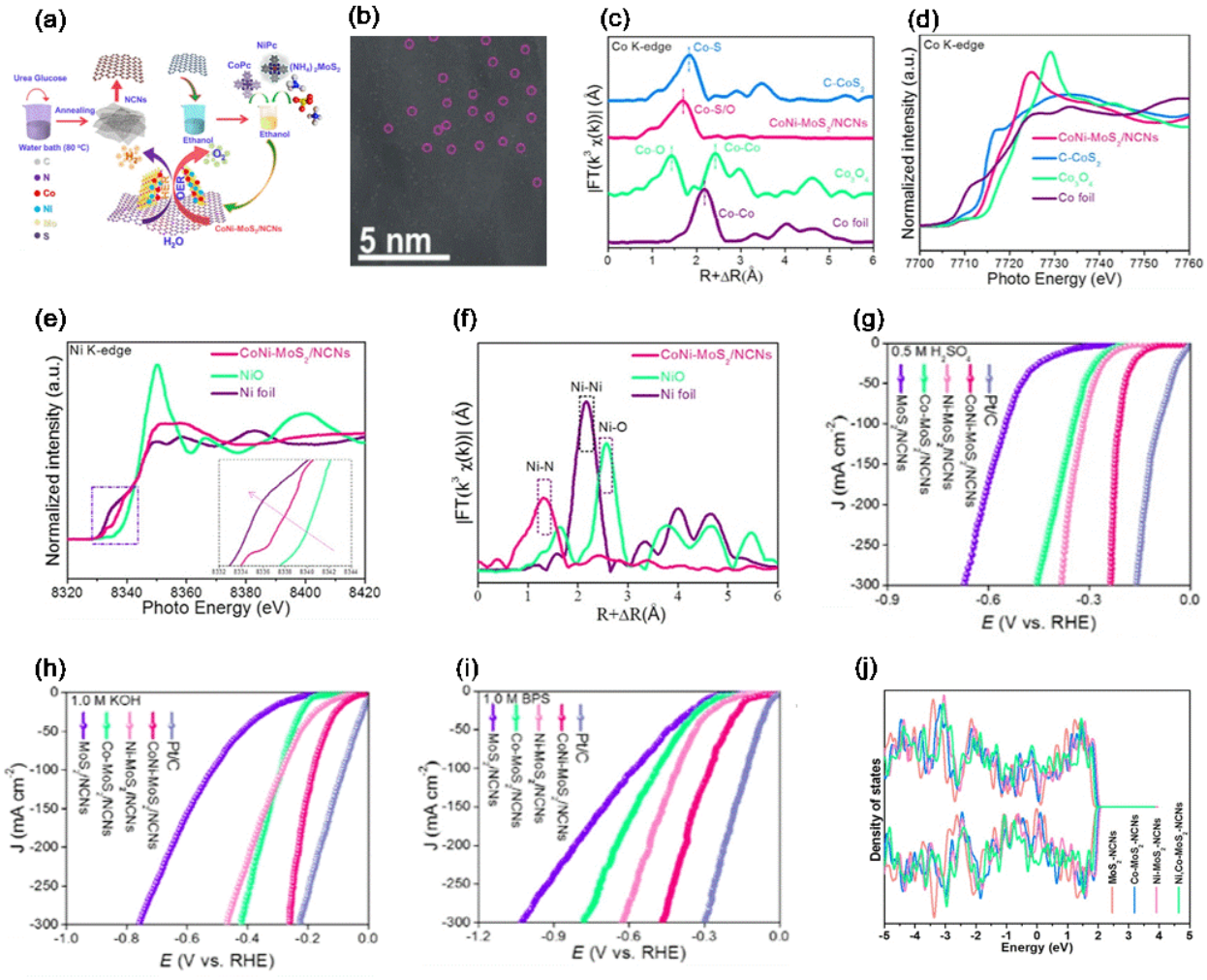

Figure 6. (a) Conceptual workflow depicting the synthesis of the CoNi-MoS_2/N-doped carbon nanoribbon hybrid (CoNi-MoS_2/NCNs). (b) Aberration-corrected spherical HAADF-STEM micrograph resolving atomically dispersed Co and Ni centers on the MoS_2/NCN matrix. (c) Fourier-transformed Co K-edge EXAFS spectra of CoNi-MoS_2/NCNs benchmarked against Co_3O_4, cubic CoS_2 and metallic Co foil. (d) Co K-edge XANES profiles for CoNi-MoS_2/NCNs and the same reference compounds. (e) Ni K-edge XANES spectra of NiO, CoNi-MoS_2/NCNs and Ni foil. (f) Corresponding Fourier-transformed Ni K-edge EXAFS curves highlighting the local

environment of Ni in the hybrid relative to the references. (g–i) iR-corrected polarization curves collected in (g) 0.5 M H_2SO_4, (h) 1.0 M phosphate-buffered saline (PBS) and (i) 1.0 M KOH, illustrating the pH-universal electrocatalytic activity. (j) DFT-calculated total density of states (TDOS) for pristine MoS_2/NCNs, single-metal-doped Co-MoS_2/NCNs and Ni-MoS_2/NCNs, and dual-metal CoNi-MoS_2/NCNs, underscoring the electronic modulation imparted by bimetallic doping. Copyright 2023, Elsevier.[91]

Dual-site catalyst design is an effective way to enhance the active site density. Figure 6 shows the spectroscopic analysis, confirming that Co and Ni atoms were successfully incorporated together into the CoNi-MoS_2 catalyst on nitrogen doped carbon nanosheets (NCNs), helping to increase the number of active sites via dual-site design. Co and Ni were atomically dispersed on the surface of MoS_2 via chemical bath deposition and pyrolysis, resulting in the formation of a CoNi-MoS_2/NCNs heterojunction, as shown in Figure 6(a). The CoNi-MoS_2/NCNs heterojunction ensured the effective dispersion of Co and Ni within the MoS_2 framework. In Figure 6(b), the CoNi-MoS_2/NCNs catalyst, as confirmed by HAADF-STEM imaging, demonstrates the successful formation of dual atomic sites, which appear as discrete bright spots without clustering. This highlights the effective atomic-level dispersion and emphasizes the crucial role of interface engineering in enhancing electrocatalytic properties. In Figure 6(c), the FT-Co K-edge EXAFS spectra reveal a shorter first-shell bond length compared to standard Co–S bonds, indicating isolated Co atoms with a unique coordination environment. Figure 6(d) shows the Co K-edge XANES spectra, confirming that the Co atoms predominantly exhibit a Co^{2+} oxidation state with mixed sulfide-oxide characteristics. In Figure 6(e), the Ni K-edge XANES spectra of the sample closely resemble that of $Ni(OH)_2$, supporting the oxidation state assignment and suggesting single-atom dispersion of Ni. Figure 6(f) provides further evidence through FT-EXAFS for Ni, showing a peak associated with Ni–O interactions and the absence of Ni–Ni bonds. This verifies that well-dispersed Ni sites achieve homogeneous dispersion of Co and Ni atoms.

Figure 6(g–i) highlights the HER performance of the catalysts across different pH environments. In Figure 6(g), in an acidic medium of 0.5 M H_2SO_4, the polarization curves with iR correction show that the CoNi-MoS_2/NCNs catalyst achieves a lower overpotential compared to reference samples, indicating superior electrocatalytic activity. In Figure 6(h), in an alkaline

medium of 1.0 M KOH, the polarization curves again reveal enhanced HER performance, with reduced onset potentials and higher current densities. In Figure 6(i), in a neutral medium of 1.0 M phosphate-buffered saline (PBS), the curves confirm that the catalyst still maintains excellent activity under pH-universal conditions. A key aspect of this excellent catalyst activity is the dual-site atomic configuration of Co and Ni; these well-dispersed atoms provide abundant active sites, facilitate efficient electron transfer, and accelerate reaction kinetics, leading to minimized overpotentials and robust HER performance across all tested media.

Figure 6(j) presents DFT-derived free energy profiles for the HER using the dual-site CoNi catalyst, indicating that the Co and Ni atoms, when atomically dispersed, synergistically reduce the energy barrier for H^* adsorption and desorption, leading to lower overpotentials. The optimized adsorption energy suggests a balanced binding strength, which is critical for efficient HER kinetics, and further confirms that the dual-site configuration enhances electron transfer and overall catalytic performance across various pH environments.[91]

4.3. Single-Atom Alloy Catalyst for Hydrogen Evolution Reaction

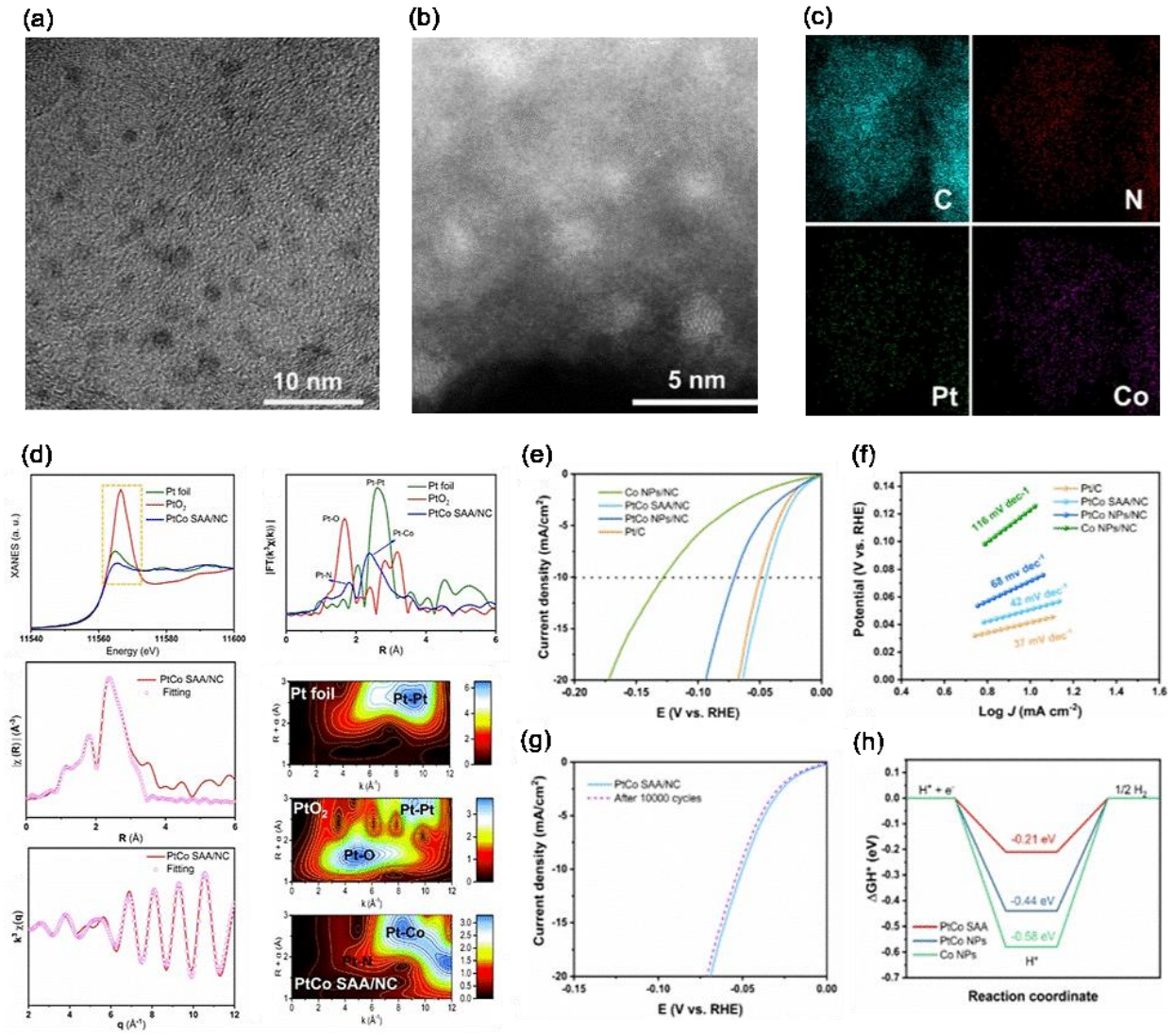

Figure 7. (a) High-resolution TEM micrographs detailing the nanoscale morphology of the PtCo single-atom alloy on N-doped carbon (PtCo SAA/NC). (b) Aberration-corrected HAADF-STEM image clearly resolving atomically isolated Pt and Co sites. (c) Elemental EDS maps (C, N, Pt, Co) confirming homogeneous spatial distribution of each component. (d) Electronic structure and local coordination of PtCo SAA/NC elucidated by Pt L_3-edge XANES and EXAFS, benchmarked against Pt foil and PtO_2; accompanying EXAFS fitting and wavelet-transform EXAFS unveil the distinctive Pt–Co environment. (e) Linear-sweep voltammograms comparing PtCo SAA/NC with Co-NP/NC, PtCo-NP/NC, and commercial Pt/C in 0.5 M H_2SO_4, highlighting the superior HER activity of the alloyed single-atom catalyst. (f) Corresponding Tafel plots derived from the polarization data, underscoring the favorable reaction kinetics of PtCo SAA/NC. (g)

Chronoamperometric durability profiles recorded after the initial cycle and following 10 000 cycles, demonstrating excellent long-term stability. (h) Density-functional-theory free-energy diagram for hydrogen evolution on PtCo SAA versus PtCo nanoparticles and Co nanoparticles, substantiating the energetic advantage conferred by the single-atom alloy architecture. Copyright 2024, Royal Society of Chemistry.[92]

A PtCo single-atom alloy supported on nitrogen-doped carbon nanosheets (PtCo SAA/NC) was synthesized through a one-step pyrolysis process that uniformly disperses ultra-small PtCo species on the carbon matrix, maximizing synergistic charge transfer in Co clusters by optimizing the utilization of Pt SA. Figure 7(a) presents high-resolution TEM images that reveal ultrasmall PtCo nanoparticles uniformly dispersed on the nanosheets without noticeable agglomeration, indicating excellent morphology and particle size uniformity. Figure 7(b) shows an AC-HAADF-STEM image that provide atomic-level evidence of the SAA structure, where isolated Pt atoms are clearly anchored on Co clusters, thus affirming the successful synthesis and homogeneous dispersion of the PtCo SAA on the carbon support. Figure 7(c) displays EDS mapping that confirms the uniform distribution of Pt, Co, N, and C elements across the nitrogen-doped carbon nanosheets. Figure 7(d) systematically details the atomic coordination and electronic structure of the PtCo SAA/NC catalyst. The Pt L_3-edge XANES spectra reveal a lower absorption edge for the catalyst compared to Pt foil and PtO_2, indicating that Pt has a negative valence state as a result of electron donation from Co. The corresponding EXAFS spectrum provides further evidence; the absence of a Pt–Pt scattering peak confirms the atomically dispersed state of Pt, while the distinct Pt–N and Pt–Co signals affirm its coordination environment. The least-squares EXAFS fitting results in R-space and q-space establish the precise coordination geometry by allowing for the quantitative extraction of bond lengths: 0.188 nm (Pt–N) and 0.259 nm (Pt–Co). Finally, WT-EXAFS analysis to further corroborate the isolated nature of the Pt atoms on Co clusters verifies the SAA formation.

Figure 7(e) presents the LSV curves, demonstrating that the PtCo SAA/NC catalyst achieves a lower overpotential compared to Co NPs/NC, PtCo NPs/NC, and even commercial Pt/C under identical conditions. Figure 7(f) shows Tafel plots where PtCo SAA/NC exhibits a Tafel slope of 42 $mV \cdot dec^{-1}$, indicative of favorable kinetics, though slightly higher than commercial Pt/C at 37

$mV \cdot dec^{-1}$ (but significantly better than other control samples). Figure 7(g) illustrates the excellent durability of the PtCo SAA/NC catalyst; it maintains stable performance even after 10,000 cycles, which emphasizes its robust stability under prolonged HER conditions. Figure 7(h) shows the density functional theory (DFT) calculated free energy diagram, which confirms that the hydrogen adsorption free energy (ΔG_{H^*}) for PtCo SAA/NC is closest to zero, supporting its high theoretical activity and efficient hydrogen evolution kinetics.[92]

5. Nobel Metal and Transition Metal SAs Electrocatalyst for Oxygen Evolution Reaction

5.1. Enhanced Adsorbate Binding via a Robust Interface Between Single Atoms and the Support

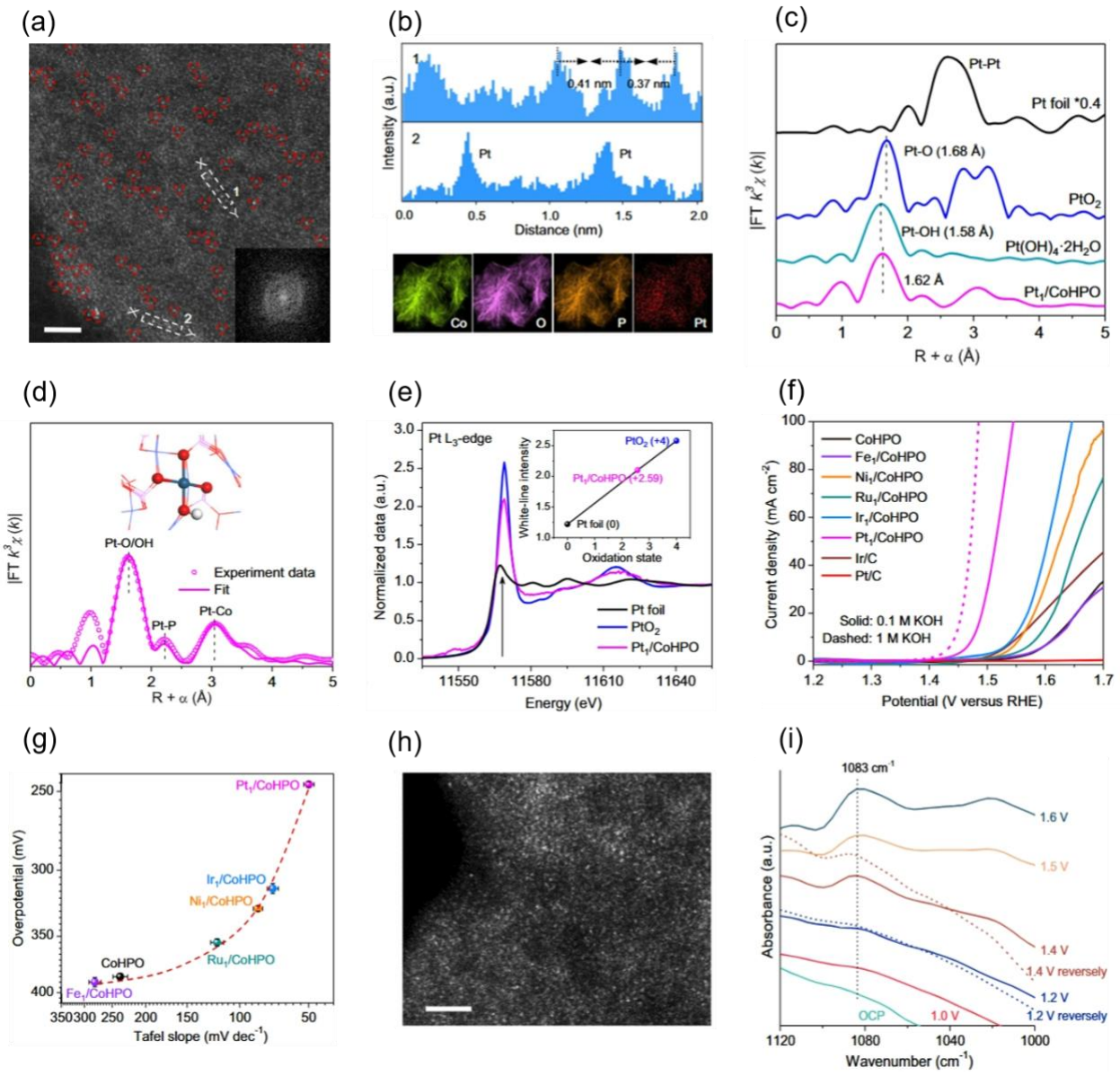

Figure 8. (a) Aberration-corrected HAADF-STEM micrograph (scale bar = 2 nm) displaying exclusively single-atom Pt sites (outlined with red dashed circles) on the CoHPO support; inset corresponding FFT pattern. (b) Atomic line-scan intensity profile with elemental-mapping overlay. (c) k^3-weighted Fourier-transformed EXAFS spectra in R-space. (d) EXAFS fitting curve; inset: optimized structural model of Pt_1/CoHPO (Pt = dark cyan, Co = blue, O = red, P = pink, H = white). (e) Pt L_3-edge XANES spectra with inset summarizing the average Pt valence state extracted from the fit. (f) Linear-sweep polarization curves for pristine CoHPO and various M_1/CoHPO analogues measured in 0.1 M and 1 M KOH. (g) OER overpotentials at 10 mA cm^{-2}

derived from the curves in (f). (h) High-resolution HAADF-STEM image of Pt_1/CoHPO after durability testing, confirming retention of isolated Pt atoms. (i) Operando potential-dependent ATR-FTIR spectra acquired for Pt_1/CoHPO. Copyright 2022, Springer Nature.[93]

The Pt_1/CoHPO catalyst exhibits exceptional OER activity and durability in alkaline media, attributed to the presence of Pt single atoms (Pt_{SAs}) with precise $Pt(OH)(O_3)/Co(P)$ coordination. HAADF-STEM images (Figure 8(a and b)) confirm the atomic dispersion of Pt on the CoHPO support, displaying isolated, bright Pt_{SAs} without any clustering. Atomic line-scanning profiles reveal a minimum interatomic distance of 0.37 nm, verifying a true single-atom distribution. XAFS analysis further corroborates a unique local environment that prevents Pt dissolution. Detailed X-ray absorption spectroscopy (XAS) elucidates the local coordination and electronic structure: The k^3-weighted FT-EXAFS spectrum in Figure 8(c) shows a prominent peak at ~1.62 Å—indicative of a mixture of Pt–O and Pt–OH bonds—while minor peaks at ~2.22 Å and ~3.05 Å correspond to Pt–P and Pt–Co bonds, respectively. EXAFS fitting (Figure 8(d)) confirms Pt coordination by three oxygen atoms and one OH in the first shell and four Co and P atoms in the second shell. Pt L_3-edge XANES (Figure 8(e)) reveals a white-line intensity corresponding to an average oxidation state of +2.59, which lies between metallic Pt and PtO_2.

Figure 8(f–h) highlights the superior electrocatalytic performance and durability of the Pt_1/CoHPO catalyst for OER in alkaline media. In Figure 8(f), the polarization curves in both 0.1 M and 1 M KOH reveal that Pt_1/CoHPO achieves significantly lower overpotentials at a current density of 10 mA cm^{-2} compared to the CoHPO support and other metal–CoHPO variants as well as benchmark catalysts like Ir/C and Pt/C. Figure 8(g) presents the quantitative analysis of these performance metrics; the Pt_1/CoHPO catalyst exhibits the lowest overpotential and Tafel slope among all tested catalysts, reflecting highly favorable OER kinetics and efficient electron transfer. Figure 8(h) shows a high-resolution HAADF-STEM image taken after durability testing, where the maintained bright contrast spots confirm that the atomically dispersed Pt_{SAs} remain intact, without agglomeration. This underscores the catalyst's robust structural stability despite the prolonged electrochemical cycling.

Figure 8(i) investigates the catalyst's operando behavior under varying applied potentials through ATR-FTIR and XAS. In Figure 8(i), the operando ATR-FTIR spectra of Pt_1/CoHPO

reveal that at 1.4 V, a prominent absorption band at approximately 1083 cm^{-1} emerges. This band, attributed to the stretching vibration of superoxide species and related to an OOH adsorbed intermediate, intensifies with increasing potential, confirming the formation of a critical reaction intermediate on the Pt sites during the OER.[93]

5.2. Controlled Assembly of Dual-Site Catalysts on a Nitrogen-Doped Carbon Matrix for Enhanced High Current Density

Figure 7 (a-b) provide high-resolution image confirming that the metal centers in the a-NiCo/NC catalyst are atomically dispersed. Elemental-mapping in Figure 9(c) reveals an even distribution of Ni and Co throughout the N-doped carbon matrix, while the accompanying AC-HAADF-STEM micrograph displays numberous bright dots, which correspond to single metal atoms, along with closely spaced pairs, indicating the formation of synergistic Ni/Co dual sites.

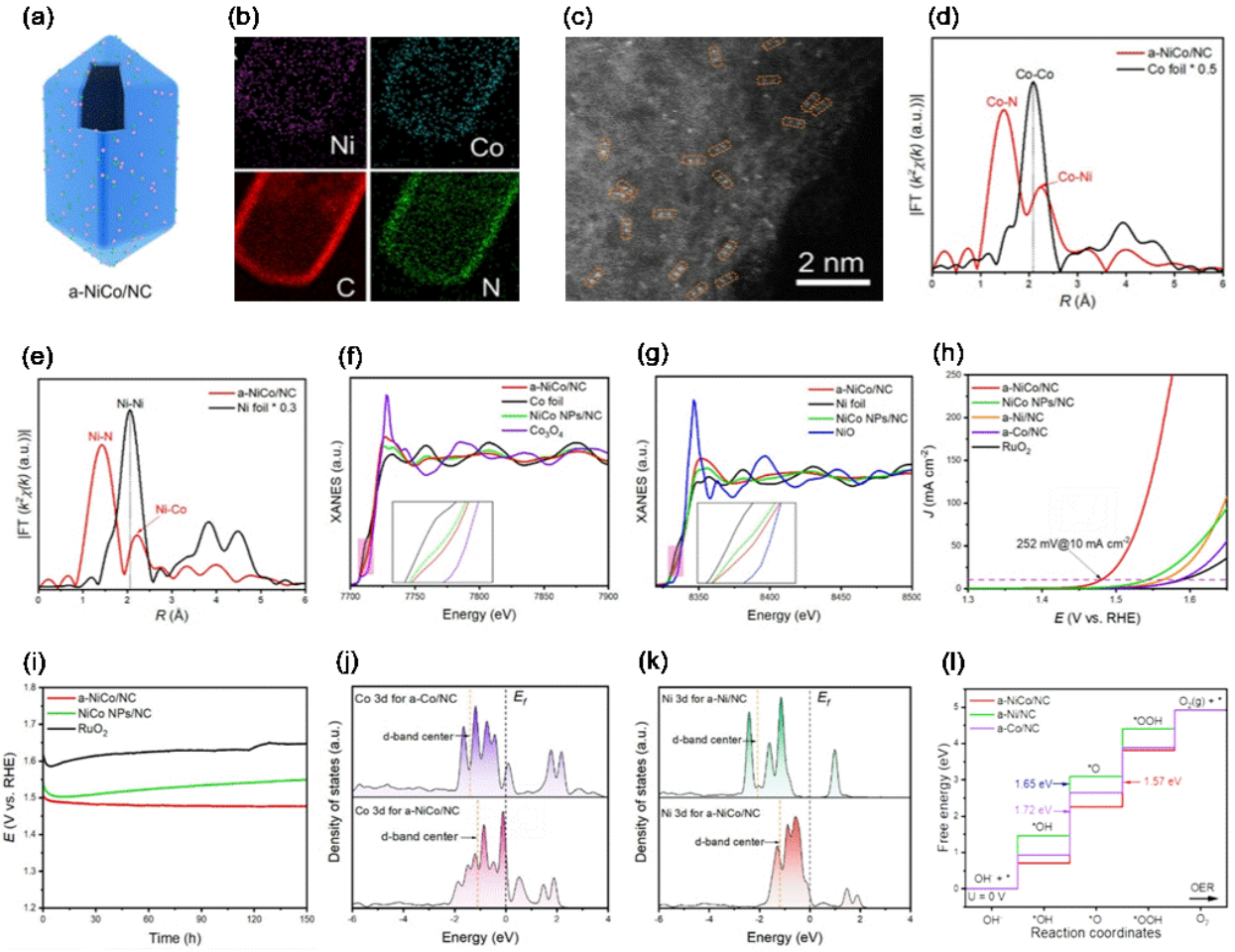

Figure 9. (a) Step-by-step schematic for constructing NiCo dual-site species embedded in N-doped carbon (NiCo/NC). (b) HAADF-STEM elemental maps confirming homogeneous Ni and Co dispersion in a-NiCo/NC. (c) Aberration-corrected HAADF-STEM micrograph highlighting atomically isolated Ni/Co pairs. (d, e) Fourier-transformed EXAFS spectra at the Co and Ni K-edges, respectively, benchmarking a-NiCo/NC against metallic Co and Ni foils. (f, g) Corresponding XANES profiles at the Co and Ni K-edges, revealing electronic structures distinct from the foil references. (h) Linear-sweep voltammogram illustrating OER activity. (i) Chronopotentiometric traces collected at 10 mA cm^{-2} for a-NiCo/NC, a-Ni/NC, and a-Co/NC, demonstrating durability under continuous operation. (j) DFT-calculated partial density of states (PDOS) for the Co3*d* orbitals in a-Co/NC versus a-NiCo/NC. (k) DFT-calculated PDOS for the Ni3*d* orbitals in a-Ni/NC versus a-NiCo/NC. (l) Computed OER free energy diagrams comparing a-NiCo/NC with its single-metal analogues, underscoring the synergistic advantage of the dual-site configuration. Copyright 2022, Wiley-VCH.[94]

Figure 9(d–g) offers detailed insight into the local electronic and coordination environment of the atomically dispersed metal sites in a-NiCo/NC using XAS. Figure 9(d) compares the FT-EXAFS spectrum at the Co K-edge for a-NiCo/NC with that of a Co foil. The prominent peak around 1.47 Å is attributed to Co–N bonds, confirming that the Co atoms are coordinated with nitrogen rather than forming metallic clusters. Figure 9(e) similarly shows the Ni K-edge FT-EXAFS spectra; a dominant peak at approximately 1.42 Å indicates the presence of Ni–N bonds, evidencing an atomic dispersion of Ni sites. Moving to the XANES analyses, Figure 9(f) displays the Co K-edge XANES spectra, where the absorption edge of a-NiCo/NC is shifted relative to the Co foil, suggesting that Co exists in an oxidized state between its metallic and oxide forms. Figure 9(g) presents the Ni K-edge XANES spectra, which likewise reveal an absorption edge positioned between that of metallic Ni and NiO. This unique coordination environment is fundamental for tuning the electronic structure and enhancing the catalytic activity for the OER.

Figure 9(h) compares LSV curves for the various catalysts, revealing the superior OER performance of a-NiCo/NC. With an onset overpotential of only ~198 mV, the catalyst sustains significantly higher current densities than both NiCo-NPs/NC and benchmark RuO_2, showing a substantial improvement in intrinsic activity. The improvement stems from atomically dispersed,

cooperative Ni/Co dual sites that tailor the local electronic structure and accelerate interfacial charge transfer. Moreover, Figure 9(i) shows potential–time responses at a steady current of 10 mA cm^{-2}, confirming the long-term electrochemical durability of the catalysts. The a-NiCo/NC catalyst maintains a nearly steady potential over an extended period, demonstrating outstanding durability in alkaline electrolyte. This stability, paired with the low overpotential in the LSV measurements, underscores the catalyst's robustness and practical applicability for efficient OER in energy conversion systems.

Figure 9(j–l) presents the DFT computational insights into the electronic structure and reaction energetics of the catalysts. The calculated partial density of states (PDOS) for Co3*d* in a-Co/NC and a-NiCo/NC is shown in Figure 9(j). The introduction of Ni into the dual-site catalyst alters the electronic structure of the Co atoms, shifting their PDOS and increasing the density of states near the Fermi level. This modification indicates improved electronic conductivity and optimized binding interactions for reaction intermediates. Figure 9(k) compares the PDOS for Ni3*d* between a-Ni/NC and a-NiCo/NC. The co-presence of Co induces a noticeable upshift of the Ni *d*-band center toward the Fermi level, suggesting a higher occupancy of antibonding states. This shift is crucial because it facilitates the adsorption and activation of key oxygen evolution intermediates. Figure 9(l) illustrates the free energy diagram for the OER over these catalysts, revealing that the rate-determining step shifts in the a-NiCo/NC catalyst, with a significantly lower energy barrier compared to the single-metal-site counterparts. Overall, the synergistic interaction between Ni and Co in a-NiCo/NC optimizes the electronic environment and accelerates the OER kinetics.[94]

5.3. Dynamic Modulation of Electronic States in Single-Atom Alloys Boosting Oxygen Evolution Reaction Stability

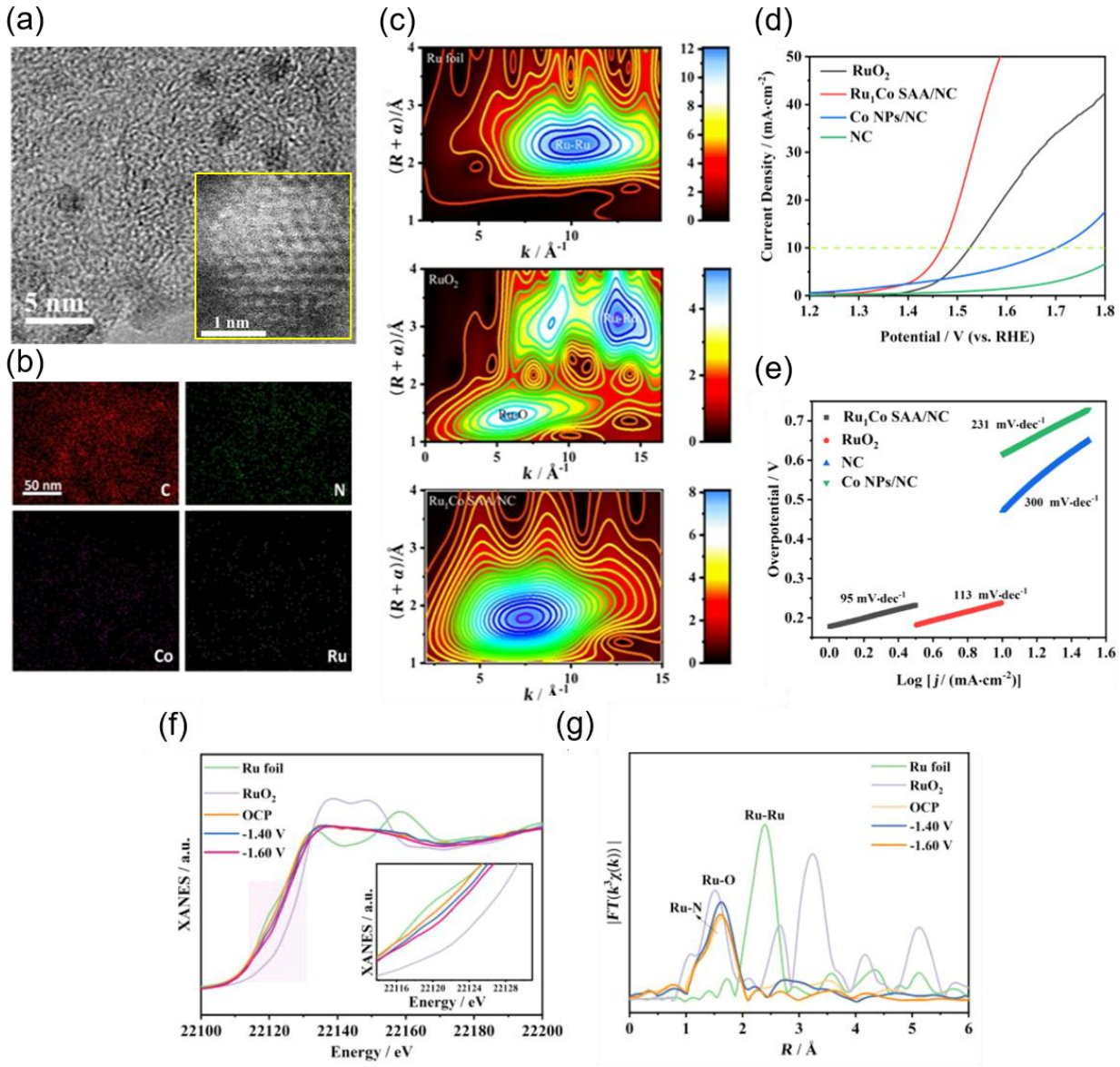

Figure 10. (a) AC-HAADF-STEM image of the Ru_1Co SAA/NC. (b) EDS mapping images (C, N, Co, and Ru elements). (c) WT-EXAFS plots of Ru foil, RuO_2, and Ru_1Co SAA/NC. (d) OER polarization curves of the Ru_1Co SAA/NC compared to reference samples. (e) Tafel plots of the Ru_1Co SAA/NC and reference samples. (f) In situ XANES under the electrochemical conditions of the Ru K-edge. (g) Ru K-edge in situ EXAFS spectra.[95]

In Figure 10(a), the HR-TEM image, taken at high magnification, shows the Ru_1Co SAA species with particle sizes ranging from approximately 1.5–4.0 nm, evidencing a narrow and

controlled size distribution. The inset of Figure 10(a) shows an AC-HAADF-STEM image, which further verifies the atomically dispersed nature of Ru species on the Co clusters. Figure 10(b) displays EDS mapping images that clearly illustrate the uniform distribution of key elements—C, N, Co, and Ru—across the nitrogen-doped ultrathin carbon nanosheets, confirming effective metal anchoring. This atomic-level insight confirms that introducing Ru does not alter the homogeneous size and morphology of the Co nanoparticles, underscoring the catalyst's optimized structural integrity and potential for enhanced electrocatalytic OER. Figure 10(c) shows the WT-EXAFS plots that compare the local bonding environments of Ru in three samples: Ru foil, RuO_2, and Ru_1Co SAA/NC. In the WT-EXAFS maps of the reference materials, two clear intensity maxima appear at approximately 2.3 $Å^{-1}$ and 1.5 $Å^{-1}$, corresponding to Ru–Ru metallic bonds and Ru–O interactions, respectively. In contrast, the Ru_1Co SAA/NC displays a single dominant intensity maximum centered around 1.4 $Å^{-1}$. This shift indicates a significant change in the local coordination sphere, confirming that Ru atoms are atomically dispersed and coordinated with nitrogen atoms rather than forming aggregated Ru–Ru clusters. The absence of any high-frequency signal near 2.3 $Å^{-1}$ proves that the synthesis successfully achieved an isolated Ru–N configuration, which is key for enhancing electrocatalytic activity in OERs.

Figure 10(d) compares the LSV-derived polarization curves of Ru_1Co SAA/NC with reference catalysts (RuO_2, Co NPs/NC, and NC) in 0.5 M H_2SO_4. The curve clearly illustrates that Ru_1Co SAA/NC achieves a current density of 10 $mA \cdot cm^{-2}$ at a notably lower overpotential of 238 mV, outperforming RuO_2 (295 mV), Co NPs/NC (470 mV), and NC (614 mV). This marked reduction in overpotential demonstrates the superior catalytic activity of the Ru_1Co SAA/NC system for OER in acidic media. Figure 10(e) complements these findings by displaying the corresponding Tafel plots. Here, the Ru_1Co SAA/NC catalyst exhibits a significantly lower Tafel slope of 95 $mV \cdot dec^{-1}$ compared to 113, 231, and 300 $mV \cdot dec^{-1}$ for RuO_2, Co NPs/NC, and NC, respectively. The reduced Tafel slope underscores the enhanced reaction kinetics and efficient charge transfer characteristics of Ru_1Co SAA/NC, confirming its potential for superior electrocatalytic performance.

Figure 10(f–g) presents in situ XAS investigations under operating electrochemical conditions to track the evolution of Ru active sites during OER. Figure 10(f) depicts the in situ Ru K-edge XANES spectra. At open-circuit voltage, the Ru valence state is intermediate, lying

between that of metallic Ru (Ru foil) and oxidized Ru (RuO_2); this is indicative of a near-zero oxidation state. As the applied potential is increased to -1.4 V versus RHE, the absorption edge shifts to higher energy, and further increases upon reaching -1.6 V, signifying progressive oxidation of Ru species. Figure 10(g) shows the corresponding in situ EXAFS spectra, where Ru–N and Ru–Co scattering paths are observed, indicating that Ru atoms remain coordinated primarily to N and Co even under reaction conditions. [95]

6. Emerging Single-Atom Catalysts Tailored for Different Types of Photoelectrodes for Solar-Assisted Water Splitting

This section discusses the integration of SACs into photoanodes and photocathodes for solar fuel production. To achieve this, the development of highly active catalysts, efficient charge transport layers, and effective passivation layers is essential. Transition-metal-based catalysts have been incorporated into photoelectrodes, demonstrating significant catalytic activity and enhanced durability. However, their performance is still insufficient for solar hydrogen production, necessitating further advances. The unique properties of SACs—such as their high catalytic activity, maximized atomic utilization, and tunable electronic structures—enable improved light absorption, charge separation, and reaction kinetics for stand-alone photoelectrochemical (PEC) systems. As a result, SAC-based photoelectrodes are emerging as a promising strategy for addressing global energy challenges.

Recent advances have demonstrated that incorporating single atoms into photoanodes such as TiO_2, $BiVO_4$, and Fe_2O_3 can significantly improve their PEC performance. The formation of M_{SA}–O–M bonds induces an electron rearrangement that enhances charge carrier separation and injection. Consequently, it is critical to design appropriate co-catalysts that accelerate charge transfer and improve photoanode stability. Studies have verified that these incorporated single atoms markedly modify the electronic structure of the photoanode, which not only promotes visible light absorption but also facilitates efficient hole transfer. Moreover, SACs can serve as true catalysts by trapping holes at the photoanode surface, providing active sites for the water oxidation reaction and thereby further enhancing the durability of the photoelectrodes. To enable the formation of SACs on photoanodes, several key criteria must be satisfied. These include the presence of anchoring sites—such as oxygen vacancies, surface defects, or heteroatoms—that can

stabilize single atoms, as well as a strong metal–support interaction to prevent atom aggregation. Additionally, the electronic structure of the photoanode should facilitate effective charge transfer between the support and the single atoms, thereby ensuring high catalytic activity.[96-98]

6.1 Mechanistic roles of SACs in photoelectrodes

6.1.1 Interface modulation: Improving the Active Sites for Surface Reactions

Interfacial engineering of photoelectrodes plays a vital role, being largely influenced by both geometric and electronic structures. Modifying the surface of supports can introduce various functional groups, coordination environments, and defect sites that enable the strong anchoring of single atoms through enhanced metal–support interactions.[99] These surface defects act as active centers for immobilizing single atoms and boosting catalytic activity. Notably, defective metal oxides and sulfides have been widely explored as SAC supports, where the synergy between the defect sites and adjacent single atoms facilitates efficient surface reactions.[100] For example, oxygen vacuums in metal oxides such as TiO_2 can stabilize single atoms of Pt, Pd, or Ru, which then serve as highly active centers for photoelectrode.

6.1.2 Charge Transfer and Separation of Photogenerated Charges

Efficient charge transfer and effective spatial separation of photogenerated carriers are crucial for achieving superior PEC performance. The incorporation of single atoms enhances these processes by promoting the separation and migration of photo-induced electrons and holes.[101] The formation of an electronic equilibrium facilitates electron transfer from the semiconductor to the metal sites through a Schottky barrier,[102] thereby improving charge transport. Such metal–support interactions in SACs play a key role in modulating carrier dynamics. For example, Pt^{2+} and Cu^{+} single atoms anchored on g-C_3N_4 shorten the electron transfer path and suppress charge recombination.[103] Likewise, embedding Pt single atom on Pt–N_3 sites into covalent triazine framework (CTF) nanosheets significantly accelerates charge mobility.[104] Moreover, Ni single atom deposited on CdS introduce mid-gap electronic states, which effectively trap photoexcited electrons and further facilitate charge transfer.[105]

6.1.3 Stability

The stability of a PEC device is a critical factor that determines its overall durability and practical applicability. Photoanodes often suffer from self-degradation caused by internal hole accumulation, which can occur more readily than the desired water oxidation reaction. Oxide-based materials generally exhibit higher resistance to photoinduced redox corrosion, whereas non-oxide semiconductors are more susceptible to degradation due to electron or hole attacks. To address this issue, protective cocatalyst layers are commonly introduced; however, these coatings increase the complexity of device fabrication.[106] Stability also has a direct impact on the cost-effectiveness of PEC systems—commercial applications require operational durability of at least 10 years, while current studies have achieved stability for only about 100 days.[107]

6.1. Single-Atom Catalysts on the TiO_2 Photoanode

Song et al. employed an *in-situ* gas-phase cation-exchange strategy to incorporate atomically dispersed Co on TiO_2 rutile nanowire photoanodes (Figure 11(a)).[96] Co substitutes for Ti without altering the morphology of the host materials due to their comparable ionic radii (Co^{2+} vs. Ti^{4+}). XANES and EXAFS analyses (Figure 11(b–c)) confirmed exclusive Co–O coordination, with no evidence of Co–Co interactions, indicating that Co is predominantly in the +2-oxidation state and integrated within the TiO_2 lattice. WT simulations (Figure 11(d)) further validated the atomic dispersion with a Co–O intensity maximum near 4.0 $Å^{-1}$. The Co/TiO_2 photoanode achieved a photocurrent density of 1.47 mA cm^{-2} at 1.23 V versus RHE—approximately 3.1 times higher than pristine TiO_2 (Figure 11(e)). This density was a result of enhanced visible light absorption, charge separation (78.7%), and transfer efficiency (94%) via a type-II homojunction (Figure 11(f)). The photoanode also exhibited ~100 h stability under varied pH conditions due to robust Co–O bonding (Figure 11(g)).

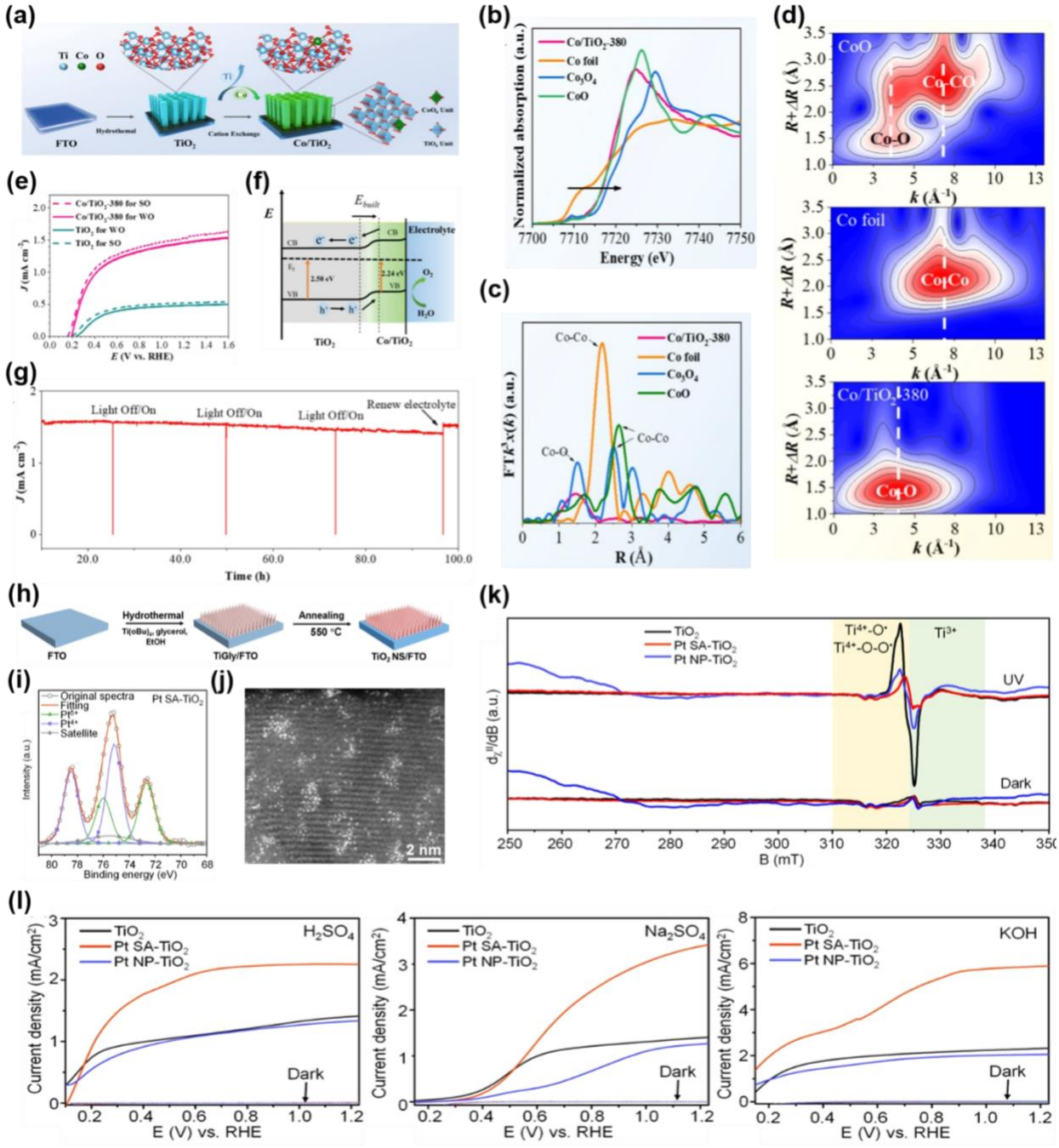

Figure 11. (a) Diagram showing the preparation process for the Co/TiO_2 photoanode. (b) Co K-edge XANES spectra. (c) Fourier-transformed magnitudes of Co K-edge EXAFS spectra of sample Co/TiO_2-380 and comparison counterparts of Co foil, CoO, and Co_3O_4. (d) Fourier-transformed magnitudes of Co K-edge EXAFS spectra of sample Co/TiO_2-380 and comparison counterparts of Co foil, CoO, and Co_3O_4. (e) J-V curves. (f) Energy band schematic diagram. (g) Long-term stability over Co/TiO_2-380 photoanode. Copyright 2023, Elsevier.[96] (h) Schematic illustration of

the synthesis procedure. (i) X-ray photoelectron spectroscopy spectra of Pt SA-TiO_2. (j) HAADF-TEM images of Pt SA-TiO_2. (k) X-band continuous wave electron paramagnetic resonance (CW EPR) spectra. (l) LSV curves of different photoanodes in 0.5 M H_2SO_4, 0.1 M Na_2SO_4, and 1 M KOH. Copyright 2020, American Chemical Society.[97]

Another study revealed uniformly dispersed Pt SAs on TiO_2 nanosheets prepared via a reactive deposition strategy (Figure 11(h)), achieving high surface density.[66] X-ray photoelectron spectroscopy (Figure 11(i)) confirmed that Pt is oxidized to $Pt^{\delta+}$ through interactions with TiO_2 defect sites (Figure 9(k)), significantly altering the electronic environment to boost catalytic activity. The Pt SAs accelerate hole transfer, reducing charge recombination and enhancing water oxidation efficiency. HAADF-STEM images (Figure 11(j)) confirmed the presence of isolated Pt SAs with a density of 3.14×10^6 Pt atoms/μm^2, and the photocurrent reached 5.89 mA cm^{-2} at 1.23 V_{RHE}—approximately 2.52 times that of bare or nanoparticle-decorated TiO_2 (Figure 11(l)). Photocurrent performance remained stable over a broad pH range. Moreover, Pal *et al.* demonstrated scalable synthesis of a Ru SA-dispersed CeO_x catalyst on Sb-doped TiO_2 nanorods.[107] By dip-coating Sb–TiO_2 nanorods with a Ru:CeO_x precursor and annealing at 200°C, Ru SAs were formed, enhancing charge separation, light absorption, and OER kinetics by band bending and the creation of new states near the Fermi level (Figures not shown here).

6.2. Single-Atom Catalysts on the $BiVO_4$ Photoanode

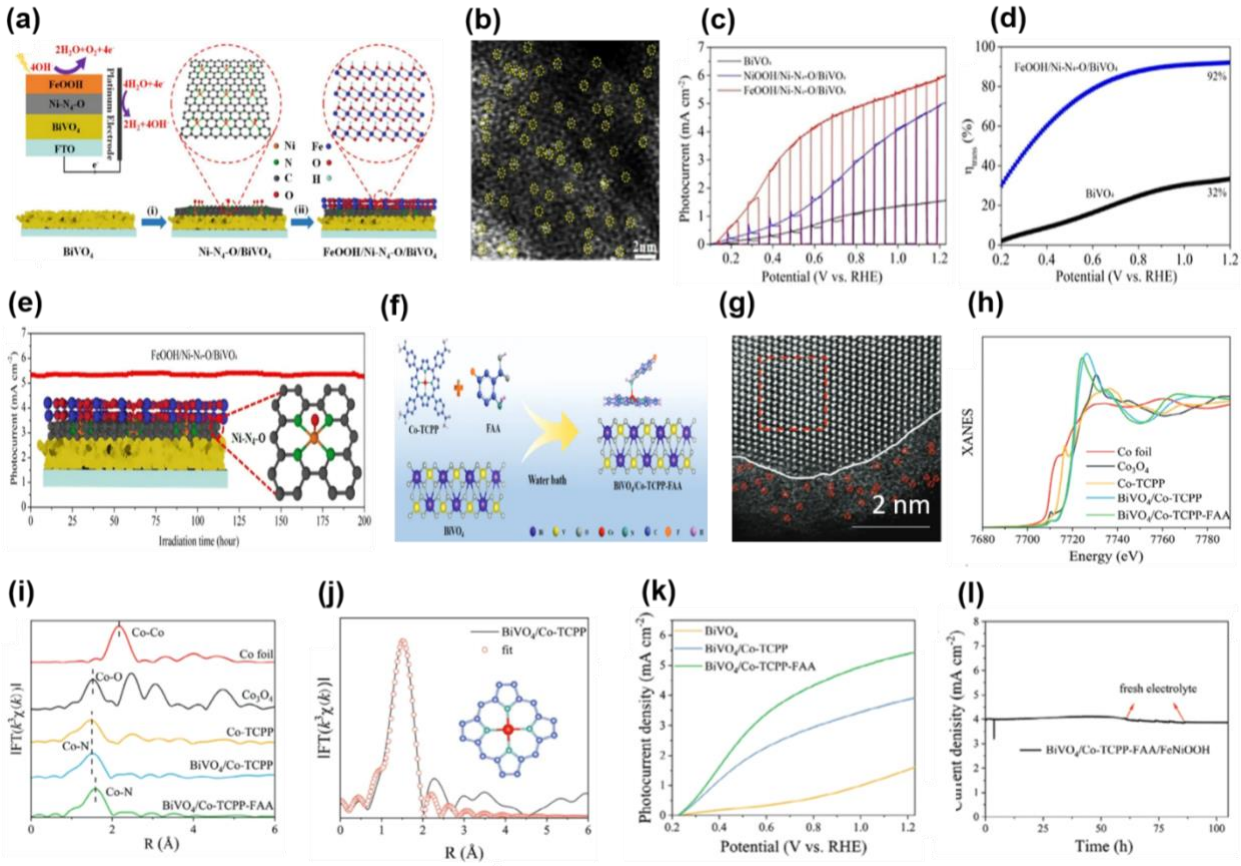

Figure 12. (a) Schematic illustration of the synthesis procedure for FeOOH/Ni-N_4-O/$BiVO_4$ array. (b) AC HAADF-STEM images of Ni-N_4-O and Ni-N_4. (c) Chopped $J-V$ curves of $BiVO_4$, Ni-N_4/$BiVO_4$, Ni-N_4-O/$BiVO_4$, NiOOH/Ni-N_4-O/$BiVO_4$, and FeOOH/Ni-N_4-O/$BiVO_4$ photoanode. (d) Charge separation efficiency of $BiVO_4$ and FeOOH/Ni-N_4-O/$BiVO_4$ photoanodes. (e) Long-term stability of FeOOH/NiN_4-O/$BiVO_4$ photoanode. Copyright 2022, American Chemical Society.[108] (f) Schematic illustration of the preparation process for $BiVO_4$/Co-TCPP-FAA photoanode. (g) HAADF-STEM images of the prepared $BiVO_4$/TCPP-FAA. (h) Co K-edge XANES spectra. (i) Co K-edge FT k^3-weighted EXAFS spectra. (j) FT-EXAFS fitting curves for $BiVO_4$/Co-TCPP in R-space. (k) LSV curves of PEC water oxidation illuminated by simulated sunlight (100 mW cm^{-2}). (l) Photocurrent stability curve for the $BiVO_4$/Co-TCPP-FAA with FeNiOOH OEC. Copyright 2024, Wiley-VCH.[109]

Single-atom Ni-N_4-O sites were synthesized (Figure 12(a)) by a coupling strategy involving carbonization, acid washing, and thermal treatment.[108] Single-atom Ni-N_4-O sites incorporated

between $BiVO_4$ photoanodes and FeOOH co-catalysts significantly enhance the photogenerated electron-hole separation (Figure 12(d)) and reaction kinetics. As a result, the $BiVO_4$ photoanode achieved a record photocurrent density (Figure 12(c)) of 6.0 mA cm^{-2} at 1.23 V versus RHE, which is 3.97 times greater than bare $BiVO_4$. Also, the Ni-N_4-O moieties were evenly distributed on $BiVO_4$, as verified by STEM (Figure 12(b)) and also supported by XAS analysis (Figures not shown here). Herein, the Ni-N_4-O sites as charge transfer layers act as bridges for efficient hole transport, reducing free energy barriers and accelerating reaction kinetics under the strong formation of Ni-O-Bi or Ni-O-V bonds. The FeOOH/Ni-N_4-O/$BiVO_4$ based PEC system demonstrated remarkable photostability (Figure 12(e)) over 200 h, and gas chromatography confirmed stoichiometric hydrogen and oxygen evolution with nearly 100% Faradaic efficiency.

Zhang et al. introduced an innovative method (Figure 12(f)) to boost the PEC efficiency of $BiVO_4$ by engineering atomic-scale noncovalent interactions through the coordination of a single Co atom with 5-fluoroanthranilic acid (FAA) as a hole-extracting layer. The Co-porphyrin complex (Co-TCPP) was first deposited onto the $BiVO_4$ substrate via a one-step water bath process, after which FAA molecules were introduced to form the $BiVO_4$/Co-TCPP-FAA photoanode. This approach dramatically increased the photocurrent density to 5.47 mA cm^{-2} at 1.23 V versus RHE (Figures 12(k-l)), primarily due to modifications in the local atomic structure around Co induced by FAA. The altered Co-TCPP configuration, optimized through noncovalent interactions, effectively reduced the charge transfer barrier at the $BiVO_4$ interface. Detailed characterizations—including X-ray absorption, electron microscopy, HAADF imaging, and XANES—reveal distinct changes in electronic configuration of Co ((Figure 12(g-j)). EXAFS analysis further indicates a transition from Co–N_4 to Co–N_5 coordination, with a Co–N bond length of 2.1 Å, thereby enhancing rapid charge transfer, reducing recombination, and significantly improving overall PEC performance.[110]

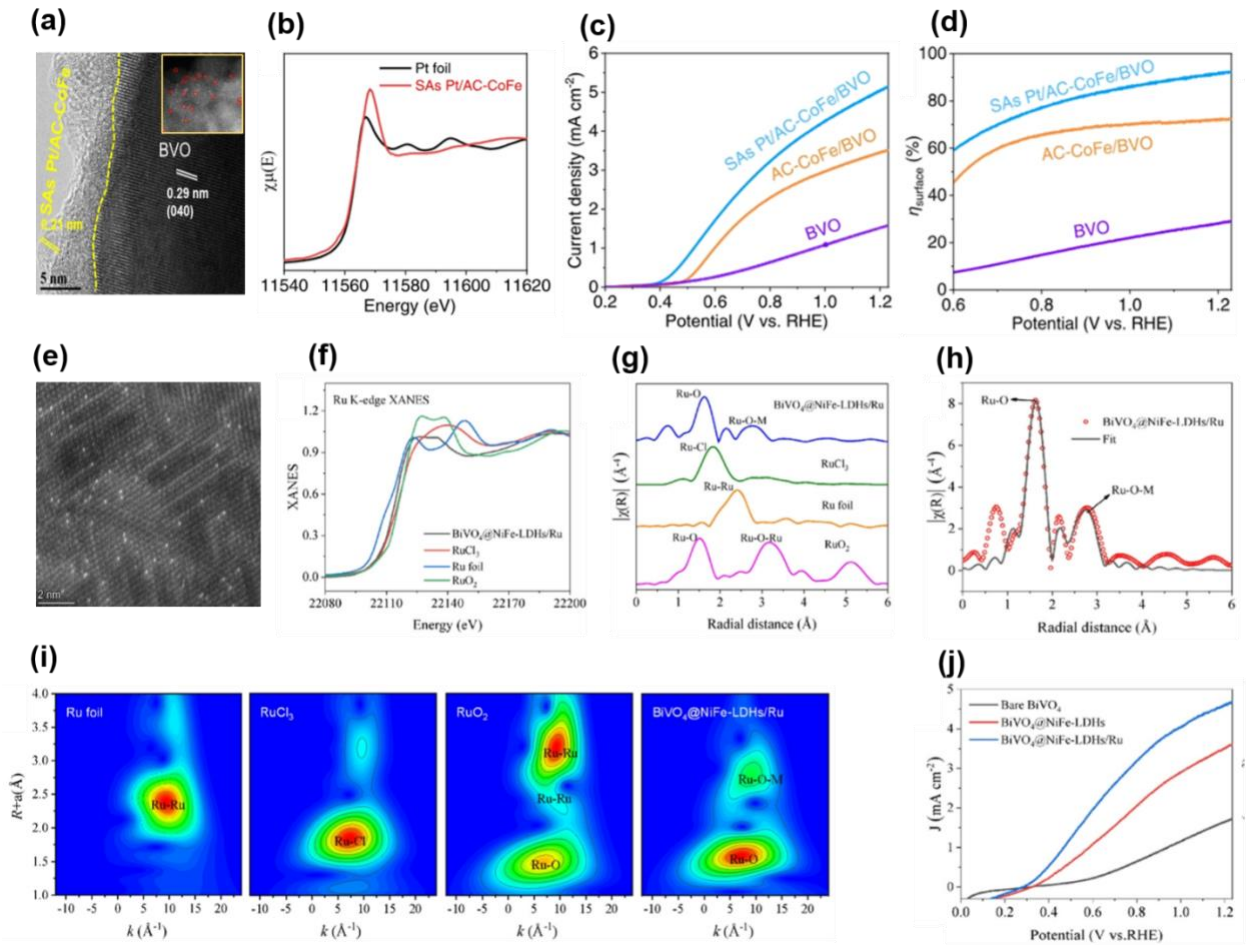

Figure 13. (a) HAADF-STEM image of SAs Pt/AC-CoFe. (b) K-edge XANES spectra of SAs Pt/AC-CoFe and Pt foil reference sample. (c) LSV curve. (d) Surface separation efficiencies ($\eta_{surface}$). Copyright 2024, Royal Society of Chemistry.[110] (e) Cs-corrected STEM images of $BiVO_4$@NiFe-LDHs/Ru photoanode. (f) XANES spectra. (g) R-space Ru K-edge EXAFS spectra. (h) EXAFS R-space fitting curve. (i) WT-EXAFS signals of Ru foil, $RuCl_3$, RuO_2, and $BiVO_4$@NiFeLDHs/Ru. (j) LSV curve of $BiVO_4$, $BiVO_4$@NiFe-LDHs, and $BiVO_4$@NiFe-LDHs/Ru. Copyright 2023, Elsevier.[111]

The Pt SAs were developed on a hybrid amorphous/crystalline cobalt-iron (CoFe) layered double hydroxide (LDH).[111] H_2PtCl_6 was introduced into ZIF-67 through a cation-exchange method, forming Pt/ZIF-67. The amorphous/crystalline CoFe LDH heterostructure provided an ideal support for Pt SAs, maintaining a stable and active catalytic surface. HAADF-STEM images

(Figure 13(a)) show the bright Pt atomic sites, which are evenly dispersed across the amorphous/crystalline CoFe LDH. XAS (Figure 13(b)) revealed that Pt atoms were embedded within the amorphous/crystalline CoFe LDH structure, optimizing its electronic properties for charge transfer (Figure 13(d)). Accordingly, the Pt/AC-CoFe catalyst exhibited a lower overpotential (230 mV at 10 mA cm^{-2}) compared to Pt-free CoFe LDH. Hence, the Pt SAs/AC-CoFe/$BiVO_4$ system achieved a high current activity of 5.14 mA cm^{-2} at 1.23 V_{RHE} under one sun illumination, a threefold improvement over bare (Figure 13(c)).

Sun et al. developed a Ru single-atom catalyst on $BiVO_4$@NiFe-LDHs through ultrasonic treatment and heating.[112] This method facilitates the *in-situ* growth of Ru atoms that are anchored to the NiFe-LDHs via Ru–O–M bonds (M = Ni or Fe), ensuring that the Ru exists as isolated atoms rather than forming clusters, as evidenced in Figure 13(e). The absence of Ru–Ru, Ru–O–Ru, and Ru–Cl bonds confirms this single-atom dispersion. Further validation comes from WT-EXAFS analysis (Figure 13(f-i)), which corroborates the isolated Ru atomic structure on NiFe-LDHs. EXAFS analysis reveals that each Ru center is coordinated by roughly 4.4 oxygen ligands, of which ~3.3 form Ru–O linkages bridged to Ni or Fe atoms. The resulting Ru–O–M (M = Ni, Fe) motifs redistribute local electron density and expedite interfacial charge transport. Benefiting from this electronic synergy, the $BiVO_4$/NiFe-LDH/Ru photoanode delivers a photocurrent of 4.65 mA cm^{-2} at 1.23 V_{RHE} significantly higher than that of pristine $BiVO_4$(1.70 mA cm^{-2}) and $BiVO_4$/NiFe-LDH (3.59 mA cm^{-2}), as depicted in Figure 13(j).

6.3. Single-Atom Alloy Integrated $BiVO_4$

Our recent work introduced a holistic strategy to enhance both the photocurrent density and long-term stability of the $BiVO_4$ photoanode. In this approach, high-surface-area, nano-leaf-like $BiVO_4$ is integrated with barium doping and semicrystalline hafnium oxide surface passivation. The nanostructured Ba:$BiVO_4$/HfO_2 photoanode was further modified by electrochemically depositing a single-atom NiPt alloy co-catalyst. As illustrated in Figure 14(a), the interface between the passivation layer and the surrounding NiPt catalyst is clearly defined. HAADF-STEM images (Figure 14(c–e)) reveal that the NiPt alloy is uniformly dispersed as isolated single atoms without any clustering; the bright spots in Figure 14(e) confirm the formation of individual metal-atom pairs. XAS analysis (Figures not shown here) validates the Pt–Ni interactions. The significant

positive shift observed in the Ni K-edge XANES spectra indicates oxidized Ni species, and FT-EXAFS peaks at ~2.1 Å confirm Ni-Ni bonds. The synergistic effect of isolated single atoms and Ni–Pt coordination markedly enhances charge transfer at the photoanode/electrolyte interface, achieving photocurrent (Figure 14(f)) densities up to 6.2 mA cm^{-2} under AM 1.5G illumination and ≈800 h of stable operation (Figure 14(g)), with no morphological deformation and superior resistance to Pt dissolution.

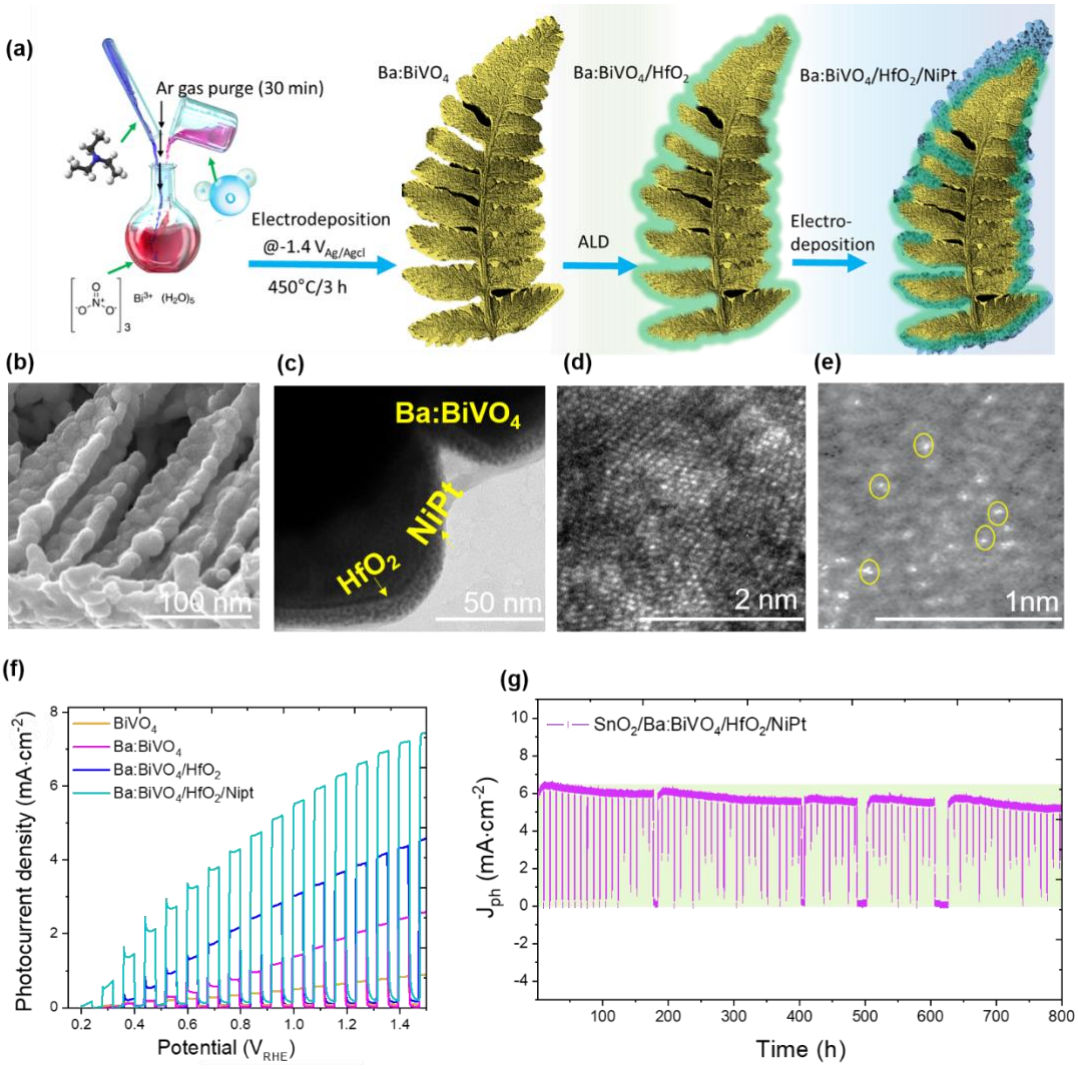

Figure 14. (a) Step-by-step schematic diagram to describe the construction of a Ba-doped $BiVO_4$ photoanode sequentially coated with an ultrathin HfO_2 passivation layer and an atomically dispersed NiPt cocatalyst. (b) FE-SEM images showing the surface architecture of the resulting Ba:$BiVO_4$/HfO_2/NiPt electrode. (c–e) Cs-corrected HAADF-STEM images verifying NiPt deposition including the isolated Pt atoms, encircled in yellow, clearly anchored to the oxide

matrix. (f) Chopped LSVs displaying the enhanced PEC response of the engineered film. (g) Chronoamperometric stability profiles recorded at 1.23 V_{RHE} demonstrating the robust long-term durability. Adapted with permission from Wiley-VCH, Copyright 2024.[113]

6.4. Single-Atom Catalysts on the *α*-Fe_2O_3 Photoanode

Wu et al. demonstrated that heterojunction engineering between Co SAs and g-C_3N_4 markedly enhances the PEC performance of *α*-Fe_2O_3.[114] In their approach, Co SAs are anchored onto g-C_3N_4 via N–C coordination bonds, as verified by XAS analysis (Figure 15(a–d)), effectively preventing aggregation. The g-C_3N_4 layer forms a heterojunction with *α*-Fe_2O_3, establishing a robust built-in electric field that improves charge separation. Upon optimization, the Co-SA/*g*-C_3N_4/Fe_2O_3 photoanode produces a photocurrent density of 1.93 mA cm^{-2} at 1.23 V_{RHE} (Figure 15(e))—a 3.22-fold enhancement over pristine *α*-Fe_2O_3. Notably, the bulk charge separation efficiency increases from 11.5% to 26.3%, while the surface efficiency rises from 40.3% to 91.3% (Figure 15(f)). Furthermore, electrons migrate from *g*-C_3N_4 to Fe_2O_3, while holes move toward Co SAs. The Co oxidation cycle (Co → Co^{2+}/Co^{3+} → O_2) functions as a key active intermediate for OER by effectively trapping holes, reducing recombination, and favorably shifting reaction thermodynamics.

Mao et al. enhanced the PEC performance of *α*-Fe_2O_3 photoanodes by depositing an ultrathin CoO_x overlayer and Ni SAs onto titanium-doped Fe_2O_3 nanorods (Figure not shown here).[74] In this configuration, the Ni SACs(Figure 15(g)), anchored via photo deposition, accelerate water oxidation kinetics by boosting the adsorption and activation of essential intermediates, while Ni–O coordination redistributes the interface charge density to improve transfer efficiency and catalytic performance. Simultaneously, the CoO_x overlayer passivates surface states, reducing carrier recombination. Theoretical calculations indicate that optimally positioned Ni SAs lower the OH adsorption free energy, enabling a more effective OER and yielding a threefold increase in photocurrent density compared to unmodified Ti:Fe_2O_3 (Figure 15(h)). A parallel study on *α*-Fe_2O_3 with a molecular Ir catalyst produced isolated Ir SAs via heterogenization and photochemical ligand removal, and transient absorption spectroscopy confirmed accelerated hole transfer, reduced hole concentration, and enhanced PEC performance.[115]

Gao et al. explored the enhancement of PEC water splitting in hematite photoanodes via doping of Pt SAs and engineered surface oxygen vacancies (O_v). Specifically, Pt SAs were incorporated into α-Fe_2O_3 using 2,2-bipyridine to chelate Pt cations, followed by annealing under Ar at 330°C to thermally remove the ligand and leave atomically dispersed Pt species (Figure 15(i)). Plasma etching subsequently generated oxygen vacancies on the Pt SAs:Fe_2O_3 photoanodes. HAADF-STEM images reveal that the Pt atoms occupy Fe sites, which is indicative of substitutional doping (Figure 15(j)). XANES spectra (Figure not shown here) revealed a valence state between Pt^0 and Pt^{4+}, confirming partial oxidation. WT-EXAFS further corroborates the presence of Pt-O and Pt-O-Fe bonds, with no Pt–Pt bonds detected, confirming single-atom dispersion. The engineered Pt SAs: Fe_2O_3-O_V photoanode achieved 3.5 mA cm^{-2} at 1.23 V_{RHE} in acidic conditions, significantly improving charge separation, carrier lifetimes, and overall efficiency.[116]

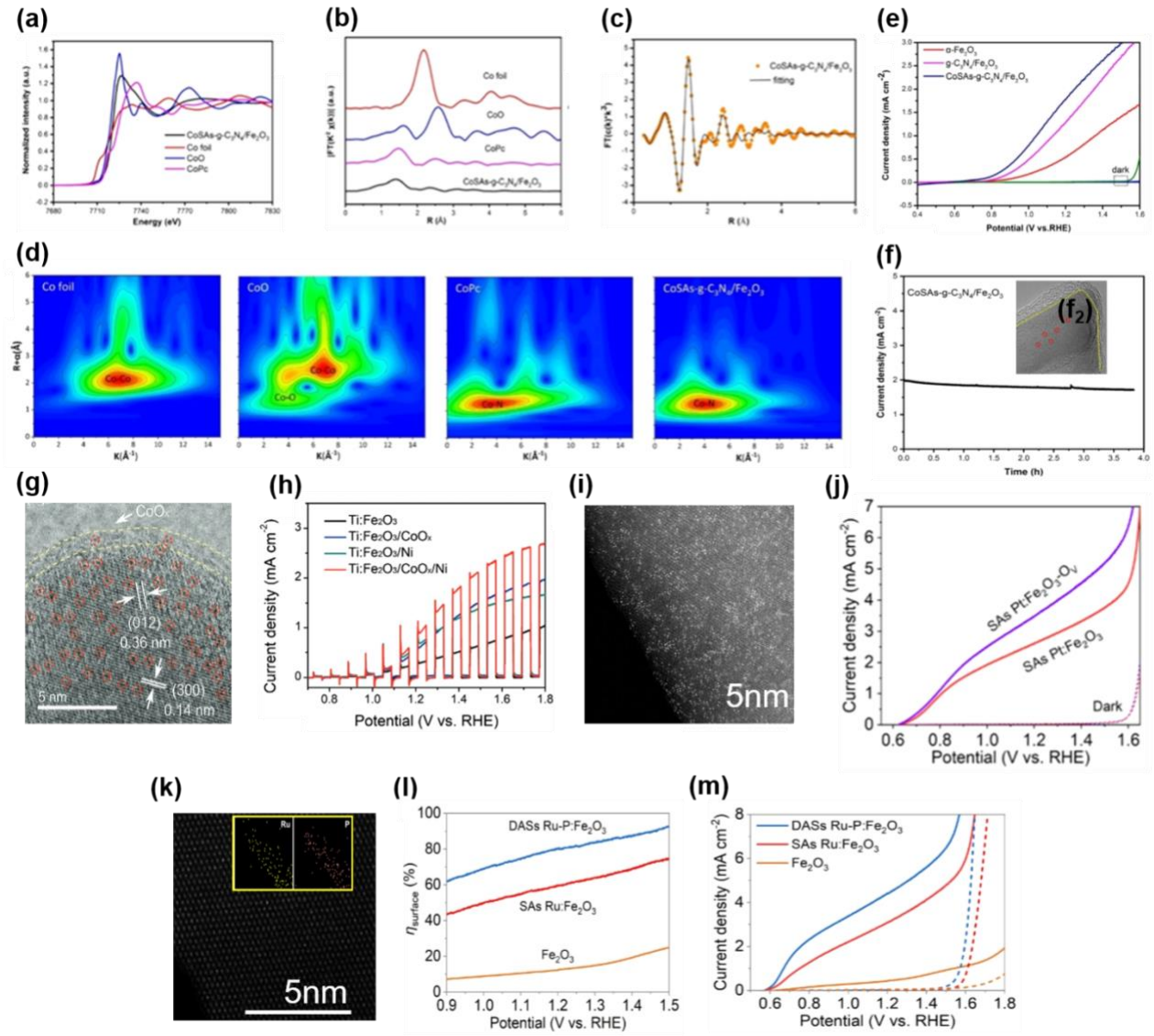

Figure 15. (a) Co K-edge XANES profiles (b) Fourier-transformed (R-space) Co K-edge EXAFS spectra (c) Least-squares fits to the EXAFS data (d) Wavelet-transformed EXAFS (WT-EXAFS) contour plots of Co foil, CoO, CoPc, and Co SAs anchored on g-C_3N_4/Fe_2O_3 (e) LSVs (f) chronoamperometric test recorded at 1 mA cm^{-2} versus RHE for the Co-SA/g-C_3N_4/Fe_2O_3 photoelectrode, with the atomic-resolution TEM including the inset (f_2) of the isolated Co atoms (red circles). Adapted with permission from the Royal Society of Chemistry, Copyright 2024 [114]. (g) High-resolution TEM micrograph of Ti-doped Fe_2O_3 coated with Ni, (h) Chopped-illumination photocurrent–potential response. Reproduced from Wiley-VCH, copyright 2022 [115]. (i) HAADF-STEM image and (j) corresponding *J–V* characteristics of the catalyst. Reprinted with permission from the American Chemical Society, Copyright 2024 [116]. (k) HAADF-STEM micrograph, (l)

Surface charge-separation efficiency ($\eta_{surface}$), and (m) *J–V* curves for the photoanode. Reproduced from the National Academy of Sciences, Copyright 2023.[117]

6.5. Single-Atom Catalysts of Diatomic Pairs on *α*-Fe_2O_3

An innovative strategy for embedding Ru–P diatomic sites (DASs) into *α*-Fe_2O_3 to enhance PEC performance.[126] AC-HAADF-STEM imaging (Figure 15(k)) reveals individual Ru atoms as bright white spots distributed on the Fe_2O_3 lattice, while STEM elemental mapping verifies the uniform dispersion of both Ru and P at the ultralow concentrations (~0.1 at.% Ru and ~0.25 at.% P), ensuring atomic-level precision without clustering. The Ru K-edge XANES spectra (Figure not shown here) indicate that Ru in the DASs exists in a valence state between Ru^0 and Ru^{4+}. A slight absorption edge shift compared to SAs Ru-doped Fe_2O_3 suggests that P incorporation modifies the electronic structure of Ru. Two distinct EXAFS peaks at 1.40 Å and 1.80 Å correspond to Ru–O and Ru–P bonds, respectively, with quantitative fitting revealing Ru–O coordination numbers of 1.6 and 2.5 (bond lengths of 2.01 Å and 2.16 Å) and a Ru–P coordination number of 1.0 (2.37 Å). WT-EXAFS analysis further confirms these bonds. Together, the low Ru doping and the formation of Ru–P bonds minimize deep electron traps, enhancing charge separation. Consequently, the DASs Ru–P:Fe_2O_3 photoanode delivers 4.2 mA cm^{-2} at 1.23 V_{RHE} (Figure 15(l-m)).

7. Photocathode with Single-Atom Catalysts

Tong et al. presented an innovative single Pt atom catalyst designed for both EC-HER and PEC-HER. Recognizing that isolated metal atoms are inherently unstable and prone to aggregation, their strategy emphasizes the necessity of anchoring these atoms onto conductive supports—such as metal oxides and carbon nitrides—via robust chemical bonds. In this study, the authors employed a partial nitridation on a porous nickel foam surface to simultaneously enhance electrical conductivity and anchoring efficacy. By forming strong Pt–N bonds, single Pt atoms can be stably captured on the Ni foam. In Figure 16(a), the Pt_1/N–Ni electrode was fabricated via a chronopotentiometric method, followed by low-temperature ammonia exposure, thereby creating a nitrogen-modified nickel framework that effectively prevents Pt aggregation. Figure 16(b) displays the interconnected three-dimensional structure of the modified Ni foam with a uniform

distribution of Pt SAs. AC-HAADF-STEM imaging (Figure 16(c)) confirmed the discrete presence of Pt atoms, marked by red circles, while XAS (Figure 16(d–e)) demonstrated a higher white-line intensity and energy shift relative to Pt foil, indicating the formation of positively charged $Pt^{\delta+}$ species. Moreover, the EXAFS data revealed a distinct Pt–N coordination peak at around 1.66 Å, in contrast to the Pt–Pt signature observed in bulk Pt. Deployed as a co-catalyst on Cu_2O nanowire photocathodes (Figure 16(f)), the Pt_1/N–Ni catalyst achieved an impressive photocurrent density of ~11.9 mA cm^{-2} at 0 V_{RHE} and a solar-to-hydrogen conversion efficiency (STH) of 1.75%. DFT calculations further confirmed that positioning Pt atoms atop the Ni layer is energetically favorable and that hydrogen adsorption on Pt_1/N–Ni is more thermoneutral than on the Pt(111) surface, thereby significantly lowering the HER overpotential.[118]

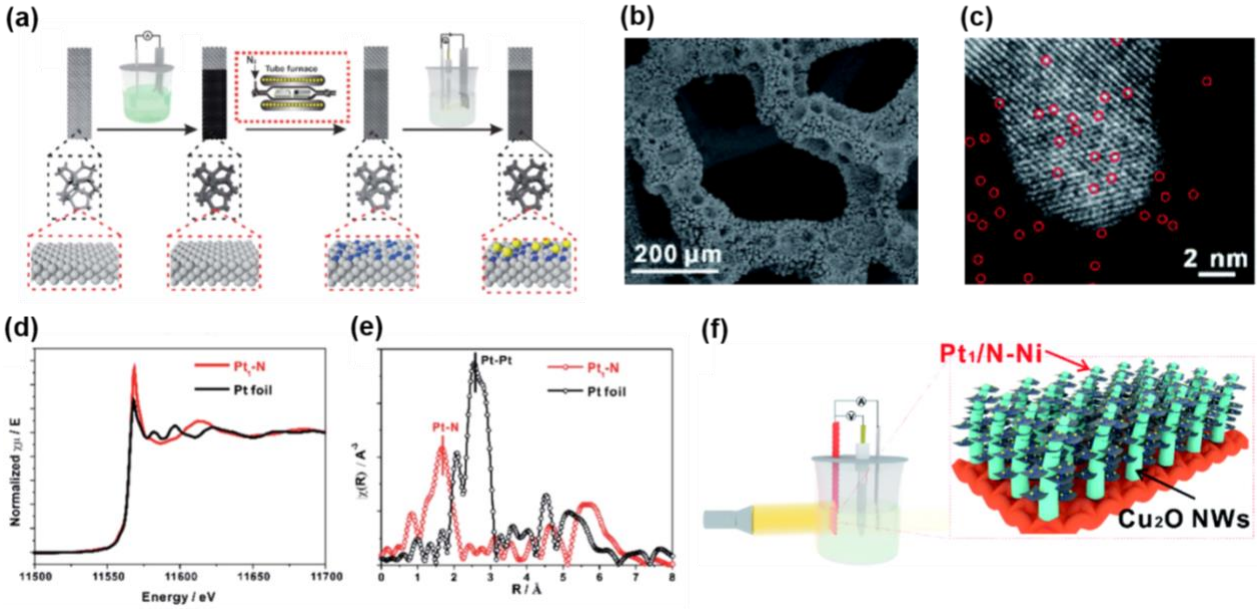

Figure 16. (a) Conceptual illustration of the synthetic pathway for single-atom Pt anchored on nitrogen-modified Ni foam (Pt_1/N–Ni/NF). (b) SEM micrographs revealing the hierarchical surface morphology of the Pt_1/N–Ni/NF scaffold. (c) Aberration-corrected HAADF-STEM image confirming atomically isolated Pt sites. (d) Pt L_3-edge XANES and (e) corresponding EXAFS spectra of Pt_1/N–Ni/NF benchmarked against bulk Pt foil. (f) Schematic of the photoelectrochemical setup used to evaluate Pt_1/N–Ni-decorated Cu_2O nanowire (NW) photoanodes. Reproduced with permission from the Royal Society of Chemistry, Copyright 2021.[118]

Based on the preceding discussion, the key findings and comparative insights have been systematically organized for clarity. A series of comprehensive tables (Tables 2–4) summarize the photo(electro)chemical water-splitting performance of representative single-atom, dual-atom, and single-atom alloy catalysts. These summaries provide an integrated perspective on the distinct catalytic behaviors, reaction pathways, and performance trends observed across different atomic configurations. In the following section, we further discuss how SACs, DACs, and SAACs differ in reaction pathways, intermediate adsorption energies, and active-site densities to elucidate the fundamental principles governing their catalytic activity.

Table 1. Summary of single –atom concentration in single-site, dual-site and alloy SACs.

Catalyst	ICP-OES (wt.%)	Reference
Single-site SACs		
C-$Ir_1/Co(OH)_2$ A-$Ir_1/Co(OH)_2$	2.0 wt% 1.2 wt%	Nat. Commun. (2020) 11, 1215
PBN-300-Ir	0.74%	Adv. Sci. (2022) 9, 2105392
$Ir_1/Cu_{0.3}Co_{2.7}O_4$	3.6 wt%	Nat. Commun. (2024) 15, 1767
Ir_1/TO-CoOOH Ir_1/VO-CoOOH	1.2% 1.3%	Nat. Commun. (2022) 13, 2473
$Ir/Ni_2P_4O_{12}$	0.56 wt%	Adv. Funct. Mater. (2024) 34, 2309824
Pd/TiO_2	0.15 wt%	Nat. Commun. (2022) 13, 2648
Pt_1/CoHPO	0.57 wt%	Nat. Commun. (2022) 13, 3822
Pt-MoS_2	0.68 wt%	Small (2022) 18, 2104824
Pt-$Ni(OH)_2$-BP	0.37 %	Small (2024) 20, 2309509
Ru/NC	11.2 wt%	Adv. Mater. (2023) 35, 2301133
Ru SAs/WC_x	1.26 wt%	J. Am. Chem. Soc. (2024) 146, 4883−4891
Ir-Co_3O_4	10.97 wt%	Adv. Mater. (2024) 2401163
$Cr_1/CoSe_2$	3.67 wt%	Adv. Mater. (2022) 34, 2200302
Fe-SA-NSFC	15.3 wt%	Nat. Commun. (2020) 11, 5892
SAC-Fe/NC	8.5 wt%	Cell Rep. Phys. Sci. (2022) 3, 100880
Ce/Zr pyrochlore monolayers	3.71 wt%	iScience (2023) 26, 107506
Cu/C_3N_4 SACs	0.47 wt%	Nat. Commun. (2023) 14, 8311

Fe-SAC@COF	1.0 wt%	Cell Rep. Phys. Sci. (2022) 3, 100804
Dual-site SACs		
NiCo-NP-NC	7.55 wt%	Nat. Commun. (2021) 12, 6766
CoNi-DSA/NG	1.09 wt%;1.80 wt%	Energy Adv. (2023) 2, 805–812
FeNiSAs/NC	0.58 wt%;0.46 wt%	ACS Appl. Mater. Interfaces (2024) 16, 18703-18712
Co/Fe-SNC800	1.18 wt%;1.66 wt% Co	Energy Environ. Sci. (2023) 16, 1685-1696
FeMo@CoNi-OH/Ni_3S_2	0.63 wt%;1.71 wt%	Chem. Eng. J. (2023) 468, 143605
FeN_4B-NiN_4B	0.58 wt%;0.81 wt%	Adv. Funct. Mater. (2024) 2315376
CeO_2 supports Pt-Pd SACs	8252 ppm;4835 ppm	Adv. Mater. (2022) 34, 2201859
Single atom alloys		
Ru_1Co SAA/NC	0.25 wt%;1.07 wt%	Chin. J. Chem. (2024) 42, 973-979
PtCo SAA	0.27 wt%;1.35 wt%.	Chem. Commun. (2024) 60, 5189–5192
CoPt-PtSA/NDPCF	0.42 wt%;13.65 wt%	Adv. Funct. Mater. (2022) 32, 2205920
$Ir_1Ni@MoO_2$	2.89 wt%	Adv. Mater. (2024) 36, 2305437
Pt-$Ni(OH)_2$ and NiPt	0.18 wt%;0.3 wt%	ACS Appl. Energy Mater. (2022) 5, 15136−15145
Ru_1Co SAA/NC	0.25 wt%;1.07 wt%	Chin. J. Chem. (2024) 42, 973-979

Table 2. Comprehensive comparison of HER and OER performances of various SAC configurations, including single-site, dual-site, and alloy catalysts.

Catalyst	**Electrolyte**	**Overpotential (mV@10 mA·cm^{-2})**	**Stability (h)**	**Reference**
HER				
C-$Ir_1/Co_{0.8}Fe_{0.2}Se_2$	1 M KOH	8	100	Nat. Commun. (2020) 11, 1215
Co-SAC	0.5 M H_2SO_4	230		Adv. Energy Mater. (2019) 9, 1803689
PBN-300-Ir	0.5 M H_2SO_4	17	36	Adv. Sci. (2022), 9, 2105392
$LaCeO_x$@NGr/Ru1	1.0 M KOH	22	30	Appl. Catal. B: Environ. (2024) 343, 123452
Rh-MoS_2-4.8	0.5M H_2SO_4	67	20	Angew. Chem. (2020) 132, 10588 –10593
Ir@$MoSe_2$@$NiCo_2Se_4$	1 M KOH	89	24	Small (2022) 18, 2200622
UP-RuNi SAs/C	1.0 M KOH	9	100	Nat. Commun. (2024) 15, 2218

Co_1/PCN	1.0 M KOH	138	24	Nat. Catal. (2019), 2, 134–141.
C_1-Pt/NiFe-LDH	1.0 M KOH	25.2	100	Nat. Commun. (2022) 13, 6875
CoNi-MoS_2/NCNs	1.0 M KOH	126.7	100	J. Mater. Sci. Technol. (2024) 178, 210–225
FeMo@CoNi-OH/Ni_3S_2	1.0 M KOH	89	30	Chem. Eng. J. (2023) 468, 143605
RuBi SAA/Bi@OG	1.0 M KOH	17.5	60	Angew. Chem. Int. Ed. (2023) 62, e202300879
RuCo@RuSACoSA-NMC	1.0 M KOH	118	2	Adv. Funct. Mater. (2023) 33, 2301804
RuNi@rGO	1.0 M KOH	15	30	New J. Chem. (2024) 48, 3942–3951
PtCo SAA/NC	0.5 M H2SO4	45	-	Chem. Commun., (2024) 60, 5189–5192
NiPt	1.0 M KOH	18	20	ACS Appl. Energy Mater. (2022) 5, 15136−15145
OER				
C-Ir_1/$Co_{0.8}Fe_{0.2}Se_2$	1 M KOH	230	100	Nat. Commun. (2020) 11, 1215
Ir_1/$Cu_{0.3}Co_{2.7}O_4$	0.1 M $HClO_4$	290	60	Nat. Commun. (2024) 15, 1767
Ir_1/V_O–CoOOH	1 M KOH	200 at 50 mA cm^{-2}	20	Nat. Commun. (2022) 13, 2473
Ir/Fe-β-$Ni(OH)_2$	1.0 m KOH	175	500	Small (2024) 2309705
Ir/$Ni_2P_4O_{12}$	1 M KOH	186	108	Adv. Funct. Mater. (2024) 34, 2309824
Ir_1/$Ni_3Fe_3S_x$	1.0 M KOH	170	350	Nat. Commun. (2022) 13, 24
IrSA-Ni_2P	1.0 M KOH	149	40	J. Am. Chem. Soc. (2021) 143, 13605−13615
Ir@$MoSe_2$@$NiCo_2Se_4$	1.0 M KOH	200	24	Small (2022) 18, 2200622
Pt_1/CoHPO	1 M KOH	209	48	Nat. Commun. (2022) 13, 3822
CoNi-MoS_2/NCNs	0.5 M H_2SO_4	67	100	J. Mater. Sci. Technol. (2024) 178, 210–225
CoNi-DSA/NG	1 M KOH	214	-	Energy Adv. (2023) 2, 805–812
Co/Fe-SNC800	1.0 M KOH	240	26	Energy Environ. Sci. (2023) 16, 1685–1696
FeMo@CoNi-OH/Ni_3S_2	1.0 M KOH	160	30	Chem. Eng. J. (2023) 468, 143605
Mg/Fe-N-C	1.0 M KOH	170	15	Angew. Chem. Int. Ed. (2023) 62, e202314303
RuNi@rGO	1.0 M KOH	240	30	New J. Chem. (2024) 48, 3942–3951
Overall water splitting				
C-Ir_1/$Co_{0.8}Fe_{0.2}Se_2$	1 M KOH	1.48	30	Nat. Commun.(2020) 11, 1215

$Ir@MoSe_2@NiCo_2Se_4$	1 M KOH	1.51 V	24	Small (2022) 18, 2200622
CoNi-MoS_2/NCNs(−,+)	1 M KOH	1.58	30	J. Mater. Sci. Technol. (2024) 178, 210–225
FeMo@CoNi-OH/Ni_3S_2 (-,+)	1 M KOH	1.48 V	75	Chem. Eng. J. (2023) 468, 143605

Table 3. Comparison of the photoelectrochemical performance of systems featuring single-atom dispersion.

Photoelectrodes	**Electrolyte**	**Phtocurrent ($mA \cdot cm^{-2}$)**	**Stability (h)**	**Reference**
Photoanaode				
α-Fe_2O_3-Ni-NC-300	1 M KOH	1.85 mA cm^{-2} at 1.23 V_{RHE}	15	Small (2020) 11, 2000577
g-C_3N_4@Co/carbon spheres	Na_2SO_4	5.08 mA cm^{-2} at 1.23 V_{RHE}	-	J. Catal. (2019) 370, 176.
Bi/TiO_2	Na_2HPO_4, NaH_2PO_4	1.65 mA cm^{-2} at 1.23 V_{RHE}	5	Nanoscale (2020) 12, 43024308.
Au/NiFeLDH/n-Si	1M NaOH	37 mA cm^{-2} at 1.23 V_{RHE}	50	Mater. Chem. A (2023) 11, 17503.
Ir/α-Fe_2O_3	0.1 MKNO_3	0.0575 mA cm^{-2} at 1.23 V_{RHE}	-	J. Am. Chem. Soc. (2023) 145, 1686.
Ir/NiO/Ni/ZrO_2/n-Si	1M NaOH	37 mA cm^{-2} at 1.23 V_{RHE}	130	Nat. Commun. (2023) 14, 609.
Co/$BiVO_4$/NC	0.1 MPBS	69 mA cm^{-2} at 1.23 V_{RHE}	-	Chem. Eng. J. (2022) 427, 131011.
Ni/Ti:Fe_2O_3/CoOx	1M NaOH	1.05 mA cm^{-2} at 1.23 V_{RHE}	-	Small (2023) 19, 2203838.
Ni N_4O/$BiVO_4$	0.5MKBi	4 mA cm^{-2} at 1.23 V_{RHE}	200	J. Am. Chem. Soc. (2021) 143, 20657.
Ir-O-Ir/Fe_2O_3	1.0M NaOH	0.8 mA cm^{-2} at 1.23 V_{RHE}	90	Nat. Commun. (2017) 8, 1341.
$BiVO_4$@NiFe-LDHs/Ru	0.5 M potassium borate	4.65 mA cm^{-2} at 1.23 V_{RHE}	5	Appl. Catal. B: Environ. (2024) 340, 123269
CoSAs–g-C_3N_4/Fe_2O_3	1 M KOH	1.93 mA cm^{-2} at 1.23 V_{RHE}	4	Chem. Sci. (2024) 15, 12973-12982
Pt_{SA}/TiO_2	0.2M PBS	2.11 mA cm^{-2} at 1.23 V_{RHE}	36000s	J. Environ. Chem. Eng. (2025) 13, 119508.
SAs Pt:Fe_2O_3-Ov	1.0 M KOH	3.65 and 5.30 mA cm^{-2} at 1.23 and 1.5 V_{RHE}	-	Nat Commun. (2023) 14, 2640.

Ba:$BiVO_4$/HfO_2/NiPt	1.0 M KOH	6.5 mA cm^{-2} at 1.23 V_{RHE}	800 h	Adv. Energy Mater. (2024) 14, 2402607.
GaAs/Pt_{SA}@NiOOH	1.0 M KOH	26.4 mA cm^{-2} at 1.23 V_{RHE}	150	Adv. Energy Mater. (2025) 25, e02953.
Photocathodes				
n^+p-Si/Ti/Ru-MoS_2	0.5 M H_2SO_4	−43 mA cm^{-2} at 0 V_{RHE}	6	Chem. Eng. J. (2021) 423, 130231.
Pt/N-Ni/Cu_2O NW	1.0M Na_2SO_4	−11.9 mA cm^{-2} at 0 V vs. RHE	3	J. Mater. Chem. A, (2021) 9, 10731.

8. Summary of Various Strategies to Optimize the Catalytic Performance: Material's Structure-Performance Relationship

SACs provide a unique opportunity to establish structure-performance relationships at a molecular level, with a precision typically associated with homogeneous catalysis. The primary challenge in this field is to successfully manipulate the coordination chemistry of the individual metal atoms without causing them to agglomerate, thereby maintaining their single-atom dispersion. One recent study demonstrated an effective synthetic strategy to achieve this. Researchers first chelated Pt cations with ethanediamine and then removed this chelating agent through rapid thermal annealing in an inert atmosphere. This method successfully decreased the Pt-O coordination number, which consequently lowered the oxidation state of the Pt. The resulting catalyst exhibited a record-high level of hydrogenation activity without any loss of selectivity. This proven ability to tune the local coordination, metal oxidation state, and catalytic performance of single atoms solidifies the role of SACs as a critical bridge between heterogeneous and homogeneous catalysis[119]. The electronic structure of SACs is fundamental to their function. The oxidation state of the metal sites, in particular, reflects the potential for electron transfer between the metal and reaction intermediates, which is directly related to the catalyst's activity in redox reactions[120]. For example, Cao et al. developed a series of Osmium (Os) SACs where they could precisely modulate the oxidation state over a wide range (from +0.9 to +2.9) by modifying the coordination environments[121]. Being able to control the oxidation state is therefore essential for understanding the structure-performance relationship and revealing the underlying mechanisms of redox reactions. However, the active central metal is not the only critical component; the coordination atoms from the support material also play an essential role in modulating the SACs' catalytic performance[122-123]. This understanding has driven intense research efforts toward the

precise design of tailored structures by engineering the coordination environment, from the first coordination shell immediately surrounding the metal to the second shell and beyond[124-125].

Specific examples highlight this strategy. Zhou et al. reported that single Pt atoms coordinated on ultrathin MOF nanosheets, forming M-N_x configurations, which notably promoted electron transfer and decreased the Gibbs free energy for adsorbed hydrogen atoms[126]. Similarly, Zhang *et al*. achieved superior electrochemical activity through the controllable synthesis of single cobalt atoms[127]. It was found that by precisely tuning a hybrid carbon/nitrogen (C/N) coordination environment, they could enhance electron transfer, thereby improving the adsorption and reaction kinetics of the intermediates.

9. Conclusion and Prospective

SACs have revolutionized (photo) electrochemical water splitting by combining atom-level dispersion, precisely runable electronic structures, and near-perfect metal utilization—key feactures that pave the way for next-generation, high-performance HER and OER catalysts. This review has outlined key advancements in the development of single-site, dual-site, and alloy SAC configurations, each offering unique advantages for enhancing catalytic activity, selectivity, and stability. Although our fundamental understanding of SACs has significantly deepened, bridging the gap between laboratory insights and real-world applications still demands further investigation. Ongoing research into these advanced architectures holds the potential for significant improvements in catalytic efficiency. However, to date, relatively few DACs and SAACs have been widely adopted in water-splitting applications. However, despite significant progress in understanding these systems at the laboratory scale, substantial challenges remain in bridging the gap to real-world applications. Future research should focus on the following areas.

First, the exact influence of the local coordination environment on the electronic structure—and thus the catalytic performance—is not yet fully understood, particularly when comparing single sites to dual or alloy sites. In-depth studies combining experimental spectroscopy and theoretical modeling can help tailor electronic interactions (e.g., *d*-band center shifts) to optimize charge transfer processes during water splitting.

Second, for catalysts featuring two proximal metal sites (dual-atom catalysts) or alloyed atoms, the cooperative effects that enhance catalytic activity are still ambiguous. The interplay

between different metal centers can either be beneficial or detrimental, depending on their arrangement and electronic communication. Moving forward, systematic studies aimed at isolating and quantifying these interactions can guide the design of dual/bimetallic catalysts that leverage synergistic effects to lower reaction barriers and improve selectivity.

Third, although DFT and other computational methods have provided valuable insights, models still often oversimplify the dynamic and complex behavior of atomically isolated sites in realistic environments. Enhanced computational models that incorporate solvent effects, dynamic electrode potentials, and complex reaction networks are required to predict catalytic activity and effectively guide experimental design.

Fourth, in situ and operando measurements under working conditions are limited by the spatial and temporal resolution required to capture the behavior of single and dual atoms during PEC water splitting. Advancing characterization methods—such as high-resolution electron microscopy under liquid conditions and time-resolved spectroscopic techniques—will enable real-time monitoring of atomic-scale changes and provide feedback on catalyst design.

Lastly, translating laboratory-scale discoveries of atomically isolated catalysts into scalable, economically viable PEC water splitting devices is still in its infancy. Issues such as synthesis cost, reproducibility at scale, and integration into complete systems remain unresolved. Addressing these challenges will be key to bridging the gap between lab-scale demonstrations and practical, scalable PEC systems for solar fuel production.

Furthermore, ongoing research challenges are predominantly centered on SAC-based catalysts, thereby limiting the scope for further advancement.

First, synthesis and design: Developing scalable and versatile synthesis strategies for SACs faces significant hurdles, including precise control of electronic and coordination structures, achieving high yet stable metal loading without aggregation, and ensuring strong metal–support interactions. Future SACs should exhibit structural robustness, tunable active sites, and adaptability to specific reaction demands while maintaining recyclability and cost efficiency.

Second, scalability: Transitioning SACs from laboratory research to industrial-scale applications remains difficult due to complex multicomponent syntheses and high production

costs. Realizing large-scale, cost-effective, and reproducible fabrication methods is therefore essential for practical deployment.

Third, mechanistic understanding: A comprehensive understanding of the atomic-level structure–activity relationship in SACs is still lacking. The limited accessibility of advanced characterization tools, such as synchrotron-based techniques, hinders this progress. Expanding the use of in situ and operando analyzes will be crucial to uncover reaction mechanisms and guide the rational design of next-generation SACs for sustainable energy systems.

Challenging Solutions and Future Directions

In situ characterization provides crucial insights into the catalytic behavior of SACs, particularly regarding active-site dynamics and their interactions with reactants. However, a comprehensive understanding of their real-time structural evolution under actual operating conditions remains limited. To overcome this limitation, future research should focus on elucidating atomic-level structure–performance relationships using well-defined model SAC systems in combination with theoretical simulations and advanced in situ/operando characterization techniques—such as high-resolution electron microscopy, X-ray absorption spectroscopy, and vibrational spectroscopies.

These integrated approaches are indispensable for revealing the true reaction pathways, identifying transient intermediates, and capturing the dynamic nature of active sites during catalysis. Furthermore, the large-scale synthesis of SACs continues to face challenges due to complex, resource-intensive, and environmentally taxing procedures. Developing more cost-effective and scalable synthesis routes—such as solvent-free, low-temperature, or electrochemical deposition strategies—will be essential to ensure the sustainable and practical deployment of SACs in real-world catalytic applications.

Acknowledgements

This research was supported by grants (2018R1A6A1A03024334, RS-2025-00523371) of the Basic Science Research Program through the National Research Foundation of Korea (NRF) and a grant (2019R1A6C1010024) of the Basic Science Research Capacity Enhancement Project through the Korea Basic Science Institute. This work was authored in part by the National Renewable Energy Laboratory for the U.S. Department of Energy under Contract Number DE-

AC36-08GO28308. Funding provided by the HydroGEN Advanced Water Splitting Materials Consortium, established as part of the Energy Materials Network under the U.S. Department of Energy, Office of Energy Efficiency and Renewable Energy, Hydrogen and Fuel Cell Technologies Office. The views expressed in the article do not necessarily represent the views of the DOE or the U.S. Government.

References

[1] K. T. Møller, T. R. Jensen, E. Akiba, H.-W. Li, *Prog. Nat. Sci.: Mater. Int*. 2017, **27** ,34-40.

[2] Q. Zhu, Y. Qu, D. Liu, K. W. Ng, H. Pan, *ACS Appl. Nano Mater.* 2020, **3**, 6270-6296.

[3] Q. Hu, K. Gao, X. Wang, H. Zheng, J. Cao, L. Mi, Q. Huo, H. Yang, J. Liu, C. He, *Nat. Commun.* 2022, **13**, 3958.

[4] X. Zou, Y. Zhang, *Chem. Soc. Rev.* 2015, **44**, 5148-5180.

[5] R. Parsons, Trans. *Faraday Soc*. 1958, **54**, 1053-1063.

[6] J. K. Nørskov, T. Bligaard, A. Logadottir, J. Kitchin, J. G. Chen, S. Pandelov, U. Stimming, *J. Electrochem. Soc.* 2005, **152**, J23.

[7] N. Danilovic, R. Subbaraman, D. Strmcnik, K. C. Chang, A. Paulikas, V. Stamenkovic, N. M. Markovic, *Angew. Chem., Int. Ed.* 2012, **51,** 12495-12498.

[8] B. Hinnemann, P. G. Moses, J. Bonde, K. P. Jørgensen, J. H. Nielsen, S. Horch, I. Chorkendorff, J. K. Nørskov, *J. Am. Chem. Soc.* 2005, **205**, 5308-5309.

[9] C. Tsai, K. Chan, J. K. Nørskov, F. Abild-Pedersen, *Surf. Sci.* 2015, **640**, 133-140.

[10] J. Kibsgaard, Z. Chen, B. N. Reinecke, T. F. Jaramillo, *Nat. Mater.* 2012, **12**, 963-969.

[11] Y. Shi, B. Zhang, *Chem. Soc. Rev.* 2016, **45**, 1529-1541.

[12] A. A. Feidenhans'l, Y. N. Regmi, C. Wei, D. Xia, J. Kibsgaard, L. A. King, *Chem. Rev*. (2024) in press.

[13] R. Subbaraman, D. Tripkovic, K.-C. Chang, D. Strmcnik, A. P. Paulikas, P. Hirunsit, M. Chan, J. Greeley, V. Stamenkovic, N. M. Markovic, *Nat. Mater.* 2012, **11**, 550-557.

[14] C. Wei, R. R. Rao, J. Peng, B. Huang, I. E. Stephens, M. Risch, Z. J. Xu, Y. Shao-Horn, *Adv. Mater.* 2019, **31**, 1806296.

[15] C. C. McCrory, S. Jung, J. C. Peters, T. F. Jaramillo, *J. Am. Chem. Soc.* 2013,**13** 16977-16987.

[16] L. Han, S. Dong, E. Wang, *Adv. Mater.* 2016, **28,** 9266-9291.

[17] B. M. Hunter, H. B. Gray, A. M. Muller, *Chem. Rev.* 2016, **116**, 14120-14136.

[18] H. Wang, H.-W. Lee, Y. Deng, Z. Lu, P.-C. Hsu, Y. Liu, D. Lin, Y. Cui, *Nat. Commun.* 2015, **6**, 7261.

[19] B. Y. Xia, Y. Yan, N. Li, H. B. Wu, X. W. D. Lou, X. Wang, *Nat. Energy* 2016, **1**, 1-8.

[20] L. Han, X.-Y. Yu, X. W. Lou, *Adv. Mater.* 2016, **28**, 4601-4605.

[21] T. Wu, S. Sun, J. Song, S. Xi, Y. Du, B. Chen, W. A. Sasangka, H. Liao, C. L. Gan, G. G. Scherer, *Nat. Catal.* 2019, **2**, 763-772.
[22] F. Hu, S. Zhu, S. Chen, Y. Li, L. Ma, T. Wu, Y. Zhang, C. Wang, C. Liu, X. Yang, *Adv. Mater.* 2017, **29**, 1606570.
[23] B. Han, K. A. Stoerzinger, V. Tileli, A. D. Gamalski, E. A. Stach, Y. Shao-Horn, *Nat. Mater.* 2017, **16**, 121-126.
[24] J. Song, C. Wei, Z.-F. Huang, C. Liu, L. Zeng, X. Wang, Z. J. Xu, *Chem. Soc. Rev.* 2020, **49**, 2196-2214.
[25] B. Qiao, A. Wang, X. Yang, L. F. Allard, Z. Jiang, Y. Cui, J. Liu, J. Li, T. Zhang, *Nat. Chem.* 2011, **3**, 634-641.
[26] A. Wang, J. Li, T. Zhang, *Nat. Rev. Chem.* 2018, **2**, 65-81.
[27] H. Jiang, W. Yang, M. Xu, E. Wang, Y. Wei, W. Liu, X. Gu, L. Liu, Q. Chen, P. Zhai, *Nat. Commun.* 2022, **13**, 6863.
[28] N. Cheng, L. Zhang, K. Doyle-Davis, X. Sun, *Electrochem. Energy Rev.* 2019, **2**, 539-573.
[29] J. Mao, C.-T. He, J. Pei, W. Chen, D. He, Y. He, Z. Zhuang, C. Chen, Q. Peng, D. Wang, *Nat. Commun.* 2018, **9**, 4958.
[30] L. Qi, J. Guan, *Adv. Funct. Mater.* 2025, **35**,2500873.
[31] Y. Qu, L. Wang, Z. Li, P. Li, Q. Zhang, Y. Lin, F. Zhou, H. Wang, Z. Yang, Y. Hu, *Adv. Mater.* 2019, **31,** 1904496.
[32] J. Xi, H. S. Jung, Y. Xu, F. Xiao, J. W. Bae, S. Wang, *Adv. Funct. Mater.* 2021, **31**, 2008318.
[33] H. Fei, J. Dong, Y. Feng, C. S. Allen, C. Wan, B. Volosskiy, M. Li, Z. Zhao, Y. Wang, H. Sun, *Nat. Catal.* 2018, **1** ,63-72.
[34] L. Qi, J. Guan, *Sci. Bull.* 2025, **70**, 1856–1871.
[35] M. Chen, J. Guan, *Adv. Funct. Mater.* 2025, 2423552.
[36] X. Xu, J. Guan, Mater. *Sci. Eng. R Rep.* 2025, **165**, 100886.
[37] L. Qi, X. Bai, Y. Wang, Z. Duan, L. Li, J. Guan, *CCS Chem.* 2025,**7**,2508–2519.
[38] X. Xu, T. Gan, J. Guan, *CCS Chem.* 2025, 1,18.
[39] Z. Zhang, C. Feng, C. Liu, M. Zuo, L. Qin, X. Yan, Y. Xing, H. Li, R. Si, S. Zhou, *Nat. Commun.* 2020, **11**, 1215.
[40] J. Fonseca, J. Lu, *ACS Catal.* 2021**, 11**, 7018-7059.
[41] S. Liu, M. Wang, X. Yang, Q. Shi, Z. Qiao, M. Lucero, Q. Ma, K. L. More, D. A. Cullen, Z. Feng, *Angew. Chem. Int. Ed.* 2020, **59**, 21698-21705.
[42] R. Xu, B. Xu, X. You, D. Shao, G. Gao, F. Li, X.-L. Wang, Y.-F. Yao*, J. Mater. Chem. A.* 2023, **11**, 11202-11209.
[43] Z. Zhang, C. Feng, D. Wang, S. Zhou, R. Wang, S. Hu, H. Li, M. Zuo, Y. Kong, J. Bao, *Nat. Commun.* 2022, **13**, 2473.
[44] Z. Lei, W. Cai, Y. Rao, K. Wang, Y. Jiang, Y. Liu, X. Jin, J. Li, Z. Lv, S. Jiao, *Nat. Commun.* 2022, **13**, 24.
[45] H. Yang, L. Shang, Q. Zhang, R. Shi, G. I. Waterhouse, L. Gu, T. Zhang, *Nat. Commun.* 2019, **10**, 4585.

[46] M. Li, M. Wang, D. Liu, Y. Pan, S. Liu, K. Sun, Y. Chen, H. Zhu, W. Guo, Y. Li, *Mater. Chem. A.* 2022, **10**, 6007-6015.
[47] H. Kang, X. Qiao, X. Jia, X. Wang, G. Hou, X. Wu, W. Qin, *Small.* 2024,2309705.
[48] X. Meng, C. Ma, L. Jiang, R. Si, X. Meng, Y. Tu, L. Yu, X. Bao, D. Deng, *Angew. Chem.* 2020, **132**, 10588-10593.
[49] Majumdar, P. Dutta, A. Sikdar, H. Lee, D. Ghosh, S. N. Jha, S. Tripathi, Y. Oh, U. N. Maiti, *Small* 2022, **18,** 2200622.
[50] Y. Guo, Y. Huang, B. Zeng, B. Han, M. Akri, M. Shi, Y. Zhao, Q. Li, Y. Su, L. Li, *Nat. Commun.* 2022, **13**, 2648.
[51] Z. Lu, B. Wang, Y. Hu, W. Liu, Y. Zhao, R. Yang, Z. Li, J. Luo, B. Chi, Z. Jiang, *Angew. Chem*. 2019, **131**, 2648-2652.
[52] A. Kumar, D. Wang, Y. Wang, Y. Jia, Y. Zhang, G. Zhang, Z. Yan, X. Sun, *Appl. Catal. B: Environ.* 2020, **274**,119091.
[53] J. Wang, Z. Huang, W. Liu, C. Chang, H. Tang, Z. Li, W. Chen, C. Jia, T. Yao, S. Wei, *J. Am. Chem. Soc.* 2017, **139**, 17281-17284.
[54] Z. Pei, X. F. Lu, H. Zhang, Y. Li, D. Luan, X. W. Lou, *Angew. Chem.* 2022, **134**, e202207537.
[55] C. Chen, M. Sun, F. Zhang, H. Li, M. Sun, P. Fang, T. Song, W. Chen, J. Dong, B. Rosen, *Energy Environ. Sci*. 2023, **16**, 1685-1696.
[56] C. C. Cheng, T. Y. Lin, Y. C. Ting, S. H. Lin, Y. Choi, S.Y. Lu, *Nano Energy* 2023, **112**,108450.
[57] J. C. Liu, H. Xiao, J. Li, *J. Am. Chem. Soc*. 2020, **142**, 3375-3383.
[58] Y. Chen, S. Ji, C. Chen, Q. Peng, D. Wang, Y. Li, *Joule* 2018, **2** ,1242-1264.
[59] L. Huo, C. Jin, J. Tang, X. Xu, K. Jiang, L. Shang, Y. Li, J. Zhang, L. Zhu, J. Chu, *ACS Appl. Energy Mater*. 2022, **5**, 15136-15145.
[60] X. Zhao, G. Wu, X. Zheng, P. Jiang, J. d. Yi, H. Zhou, X. Gao, Z. Q. Yu, Y. Wu, *Angew. Chem. Int. Ed*. 2023, **62**, e202300879.
[61] Z. Deng, Z. Sun, Y. Li, J. Pei, W. Chen, *Chin. J. Chem*. 2024, **42**, 973-979.
[62] X. Wang, H. Yao, C. Zhang, C. Li, K. Tong, M. Gu, Z. Cao, M. Huang, H. Jiang, *Adv. Funct. Mater*. 2023, **33**, 2301804.
[63] Y. Ren, Y. Tang, L. Zhang, X. Liu, L. Li, S. Miao, T. Zhang, *Nat. Commun.* 2019, **10**, 4500.
[64] Y. Chen, S. Ji, S. Zhao, W. Chen, J. Dong, W. C. Cheong, R. Shen, X. Wen, L. Zheng, A. I. Rykov, S. Cai, *Nat. Commun.* 2018, **9**, 5422.
[65] Y. Xie, Y. Sun, H. Tao, X. Wang, J. Wu, K. Ma, L. Wang, Z. Kang, Y. Zhang, *Adv. Funct. Mater*. 2022, **32**, 2111777.
[66] J. Han, J. Sun, S. Chen, S. Zhang, L. Qi, A. Husile, J. Guan, *Adv. Mater*. 2024, **36**, 2408139.
[67] C. Hu, Y. Hu, B. Zhang, H. Zhang, X. Bao, J. Zhang, P. Yuan, *Electrochem. Energy Rev.* 2024, **7**, 19.
[68] Qian, J. Zeng, S. Zhao, Q. Zheng, J. Tian, Q. Xu, H. Zhang, J. Li, *Nano Mater. Sci.* 2024, *doi.org/10.1016/j.nanoms.2024.03.006*

[69] B. Wu, T. Sun, Y. You, H. Meng, D. M. Morales, M. Lounasvuori, A. Beheshti Askari, L. Jiang, F. Zeng, B. Hu, X. Zhang, R. Tai, Z. J. Xu, T. Petit, L. Mai, *Angew. Chem. Int. Ed.* 2023, **62**, 202219188.
[70] Z. Liu, N. Zhang, Y. Xiong, *J. Phys. Chem. C* 2024, **128**, 13651–13665.
[71] C. Hu, Y. Hu, B. Zhang, H. Zhang, X. Bao, J. Zhang, P. Yuan, *Electrochem. Energy Rev.* 2024, **7**, 19.
[72] J. Huang, Y. Li, Y. Zhang, G. Rao, C. Wu, Y. Hu, J. Xiong, *Angew. Chem*. 2019, **131**, 17619–17625.
[73] F. Gong, Y. Liu, Y. Zhao, W. Liu, G. Zeng, G. Wang, J. Liu, *Angew. Chem. Int. Ed.* 2023, **62**, e202308091.
[74] J. Zhang, J. Liu, L. Xi, Y. Yu, N. Chen, S. Sun, W. Wang, K. M. Lange, B. Zhang, and *J. Am. Chem. Soc.* 2018, **140**, 3876–3879.
[75] M. A. Deshmukh, A. Bakandritsos, R. Zbořil, *Nano-Micro Lett.* 2025,**17**, 1.
[76] L. Cao, Q. Luo, W. Liu, Y. Lin, X. Liu, Y. Cao, W. Zhang, Y. Wu, J. Yang, T. Yao, S. Wei, *Nat. Catal.* 2019, **2**, 134–141.
[77] S. Fang, X. Zhu, X. Liu, J. Gu, W. Liu, D. Wang, W. Zhang, Y. Lin, J. Lu, S. Wei, Y. Li, T. Yao, *Nat. Commun.* 2020, **11**,1029.
[78] Y. Yang, Y. Wang, Y. Xiong, X. Huang, L. *Chem. Soc.* 2019,**141**,1463–1466.
[79] M. A. Bañares, *Catal. Today* 2007, **126**, 1.
[80] L. DeRita, J. Resasco, S. Dai, A. Boubnov, H. V. Thang, A. S. Hoffman, I. Ro, G. W. Graham, S. R. Bare, G. Pacchioni, X. Pan, P. Christopher, *Nat. Mater.* 2019, **18**, 746.
[81] Y. Chen, T. Kasama, Z. Huang, P. Hu, J. Chen, X. Liu, X. Tang, *Chem. Eur. J.* 2015, **21**, 17397
[82] M.L Grant, BS Swartzentruber, NC Bartelt, JB Hannon, *Phys. Rev. Lett.* 2001, **86**, 4588.
[83] S. Wei, A. Li, J. C. Liu, Z. Li, W. Chen, Y. Gong, Q. Zhang, W. C. Cheong, Y. Wang, L. Zheng, H. Xiao, C. Chen, D. Wang, Q. Peng, L. Gu, X. Han, J. Li, Y. Li, *Nat. Nanotechnol.* 2018, **13**, 856.
[84] F. Wang, X. Zhao, Y. Li, L. Liang, K. Sasaki, Q. Hao, W. Yuan, S. Li, H. Liu, *Appl. Catal. B Environ.* 2024, **348**, 123830.
[85] Z. Pu, I.S. Amiinu, R. Cheng, P. Wang, C. Zhang, S. Mu, W. Zhao, F. Su, G. Zhang, S. Liao, S. Sun, *Nano-Micro Lett.* 2020, **12**, 21.
[86] Z. Geng, Y. Liu, X. Kong, P. Li, K. Li, *Adv. Mater.* 2018, **30**,1803498.
[87] C. Ling, L. Shi, Y. Ouyang, X. C. Zeng, J. Wang, *Nano Lett.* 2017, **17**, 5133–5139.
[88] M. Yang, J. Wang, P. Dai, X. Tang, G. Li, L. Yang, *New J. Chem*. 2024, **48(9)**, 3942-3951.
[89] Lin, X., Hu, W., Xu, J., Liu, X., Jiang, W., Ma, X.,Wu, Y. *J. Am. Chem. Soc.* 2024, **146**, 4883-4891.
[90] R. Yao, K. Sun, K. Zhang, Y. Wu, Y. Du, Q. Zhao, J. Li, *Nat. Comm.* 2024, **15**, 2218.
[91] I. Khan, Y. Chen, Z. Li, W. Liu, S. Khan, S. Ullah, L. Yang, *J. Mat. Sci. & Tech* 2024, **178**, 210-225.

[92] X. Niu, H. Geng, Z. Lv, J. Wei, D. Xu, W. Chen, *Chem. Comm.* 2024, **60**, 5189-5192.
[93] L. Zeng, Z. Zhao, F. Lv, Z. Xia, S. Y. Lu, J. Li, S. Guo. *Nat. Comm.* 2022, **13**,3822.
[94] Z. Pei, X. F. Lu, H. Zhang, Y. Li, D. Luan, X. W. Lou, *Angewandte Chem.* 2022, **134(40)**, e202207537.
[95] Z. Deng, Z. Sun, Y. Li, J. Pei, W. Chen, *Chin. J. Chem.* 2024, **42**, 973-979.
[96] K. Song, H. Hou, D. Zhang, F. He, W. Yang, W. *Appl. Catal. B: Environ.* 2023, **330**,122630.
[97] W. Q. Han, Z. H. Liu, Y. B. Pan, G. N. Guo, J. X. Zou, Y. Xia, Z. M. Peng, W. Li, A. G. Dong, *Adv. Mater.* 2020, **32**, 2002584.
[98] Q. Ding, B. Song, P. Xu, S. Jin, *Chem.* 2016, **1**, 699.
[99] T. Ling, M. Jaroniec, S. Z. Qiao, *Adv. Mater.* 2020, **32**, 2001866.
[100] S. K. Deng, B. W. Zhang, P. Choo, J. M. Smeets, T. W. Odom, *Nano Lett.* 2021, **21**, 1523.
[101] H. Wang, J. M. Chen, Y. P. Lin, X. H. Wang, J. M. Li, Y. Li, L. J. Gao, L. B. Zhang, D. L. Chao, X. Xiao, J. M. Lee, *Adv. Mater.* 2021, **33**, 2008422.
[102] Y. O. Wang, F. Silveri, M. K. Bayazit, Q. S. Ruan, Y. M. Li, J. J. Xie, C. R. Catlow, J. W. Tang, *Adv. Energy Mater.* 2018, **8**, 1801084.
[103] J. Wang, Y. C. Sun, J. W. Lai, R. H. Pan, Y. L. Fan, X. W. Wu, M. Ou, Y. S. Zhu, L. J. Fu, F. F. Shi, Y. P. Wu, *Nanoscale Adv.* 2021, **3**, 1876.
[104] F. Nandjou, S. Haussener, *J. Phys. D: Appl. Phys.* 2017, **50**, 124002.
[105] Z. Wang, Y. Cheng, S. Wang, J. Xu, B. Peng, D. Luo, L. Ma, *Nano Res.* 2023, **16**, 9335.
[106] S. Wu, M. L Wu, N. Denisov, Z. Badura, G. Zoppellaro, X. Y. Yang, X. Y, P. Schmuki, *J. Am. Chem. Soc.*2020, 164(20), 16363-16368.
[107] D. Pal, D. Mondal, D. Maity, D. De, M. K. Ganesha, A. K. Singh, G. G. Khan, *J. Mater. Chem. A,* 2024, **12**, 3034-3045.
[108] X. Zhang, P. Zhai, Y. Zhang, Y. Wu, C. Wang, L. Ran, J. Hou, *J. Am. Chem. Soc.* 2021,**143**, 20657-20669.
[109] C. Zhang, Y. Wang, W. Sun, Z. Hua, Z. Zhang, S. Gong, Y.Tian, *Adv. Mater.* 2024, 37(4), 2410632.
[110] S. Xia, F. Xu, B. Weng, *J. Mater. Chem. A,* 2024, **12**, 4635-4642.
[111] M. Gao, N. T. Nguyen, R. T. Gao, X. Liu, X. Zhang, L. Wang, *Appl. Catal. B: Environ.* 2023, **336**, 122920.
[112] Y. Sun, H. Li, Y. Hu, J. Wang, A. Li, P. F. X. Corvini, *Appl. Catal. B: Environ.* 2024, **340**, 123269.
[113] M. Arunachalam, K.S. Lee, K. Zhu, S. H. Kang. *Adv. Energy Mater*. 2024, **13,** 2402607.
[114] J. Wu, X. Du, M. Li, H. Chen, B. Hu, H. Ding, W. Liu, *Chem. Sci.* 2024, **15**, 12973-12982.
[115] L. Mao, Y. C. Huang, H. Deng, F. Meng, Y. Fu, Y. Wang, S. Shen, S. *Small*, 2023, **19** 2203838.

[116] Q. Guo, Q. Zhao, R. Crespo-Otero, D. Di Tommaso, J. Tang, S. D. Dimitrov, A. B. Jorge Sobrido, *J. Am. Chem. Soc.* 2023, **145**,1686-1695.
[117] S. Tong, B. Fu, L. Gan, Z. Zhang, *J. Mater. Chem. A*. 2021, **9**, 10731-10738.
[118] B. Zhao, X. Huang, Y. Ding, Y. Bi, *Angew. Chem. Int. Ed.* 2023, **62**, 202213067.
[119] D. Cao, H. Xu, H. Li, C. Feng, J. Zeng, D. Cheng, *Nat. Commun.* 2022, **13**, 5843.
[120] X. Rong, H. J. Wang, XL Lu, R. Si, T. B. Lu, *Angew. Chem. Int. Ed.* 2020, **59**, 1961–1965.
[121] Jiao, J. Wang, H. L. Jiang, *Acc. Mater. Res.* 2021, **2**, 327–339.
[122] X. Rong, H. J. Wang, XL Lu, R. Si, T. B. Lu, *Angew. Chem. Int. Ed.* 2020, **59,** 1961–1965.
[123] L. Jiao, J. Wang, H. L. Jiang, *Acc. Mater. Res*. 2021, **2,** 327–339.
[124] Q. Zuo, T. Liu, C. Chen, Y. Ji, X. Gong, Y. Mai, Y. Zhou, *Angew. Chem. Int. Ed.* 2019, **58**, 10198–10203.
[125] Z. L. Wang, X. F. Hao, Z. Jiang, XP. Sun, D. Xu, J. Wang, H. X. Zhong, F. L. Meng, X. B. Zhang, *J. Am. Chem. Soc.* 2015, **137**,15070–15073.
[126] ES Avraham, B. Malik, A. Yarmolenko, R. Konar, S. Remennik, G. C. Taguri, S. Zorzi, E. Cattaruzza, MY Hubner, G. D. Nessim, *J. Mater. Chem. A* 2024, **12,** 26749–26761.
[127] J. Liang, X. Yang, C. Xu, T. Zhang, J. Li, Chin. J. Catal. 2017, **38**, 1566–1573.